Cell Reports
Medicine

Article

Targeting MCL1-driven anti-apoptotic pathways overcomes blast progression after hypomethylating agent failure in chronic myelomonocytic leukemia

Graphical abstract

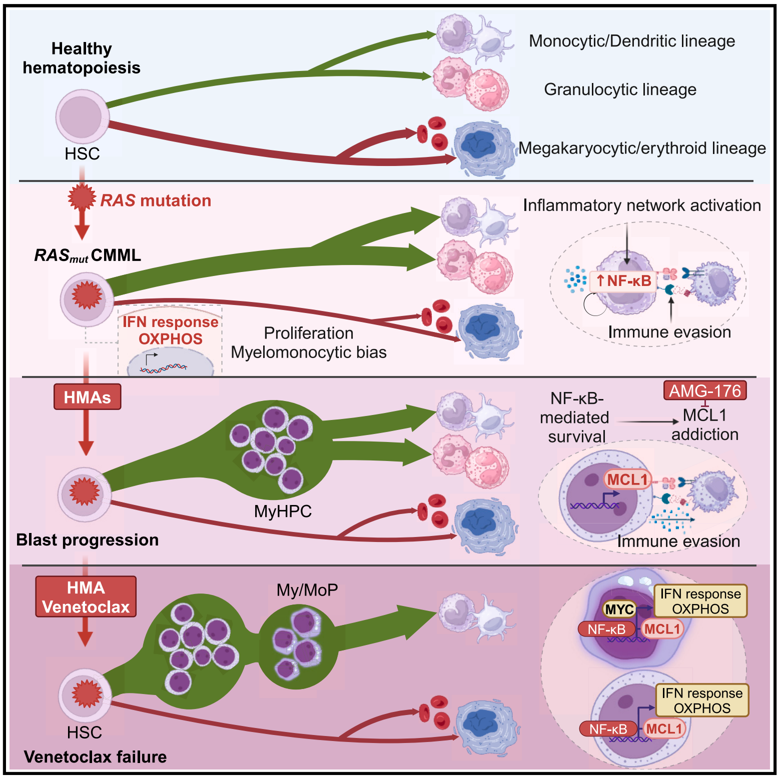
Healthy hematopoiesis
HSC
Monocytic/Dendritic lineage
Granulocytic lineage
Megakaryocytic/erythroid lineage
RAS mutation
RAS$_{mut}$ CMML
Inflammatory network activation
↑NF-κB
Immune evasion
IFN response
OXPHOS
Proliferation
Myelomonocytic bias
HMAs
NF-κB-mediated survival
AMG-176
MCL1 addiction
MCL1
MyHPC
Immune evasion
Blast progression
HMA
Venetoclax
My/MoP
MYC
IFN response
OXPHOS
NF-κB
MCL1
IFN response
OXPHOS
NF-κB
MCL1
HSC
Venetoclax failure

Highlights

- *RAS* mutations induce inflammatory network activation and immune evasion in CMML
- Expansion of NF-κB-dependent HSPCs drives blast progression (BP) after HMA therapy
- *RAS* mutant CMML HSPCs rely on MCL1 for survival during BP
- NF-κB pathway activation in *RAS* mutant HSPCs drives venetoclax resistance

Authors

Guillermo Montalban-Bravo,
Natthakan Thongon,
Juan Jose Rodriguez-Sevilla, ...,
Hagop Kantarjian,
Guillermo Garcia-Manero, Simona Colla

Correspondence

scolla@mdanderson.org

In brief

In brief, Montalban-Bravo et al. show that *RAS* pathway mutations induce multi-step reprogramming of distinct cellular populations in CMML. Expansion of myeloid progenitors at blast progression following hypomethylating agent therapy is driven by NF-κB pathway activation and MCL1 dependency. These data support the potential of NF-κB-targeted therapies in CMML.

Montalban-Bravo et al., 2024, Cell Reports Medicine *5*, 101585
June 18, 2024 © 2024 The Authors. Published by Elsevier Inc.
https://doi.org/10.1016/j.xcrm.2024.101585

Cell Reports Medicine

CellPress
OPEN ACCESS

Article

Targeting MCL1-driven anti-apoptotic pathways overcomes blast progression after hypomethylating agent failure in chronic myelomonocytic leukemia

Guillermo Montalban-Bravo,[1,7] Natthakan Thongon,[1,7] Juan Jose Rodriguez-Sevilla,[1,7] Feiyang Ma,[2] Irene Ganan-Gomez,[1] Hui Yang,[1] Yi June Kim,[1] Vera Adema,[1] Bethany Wildeman,[1] Tomoyuki Tanaka,[1] Faezeh Darbaniyan,[3] Gheath Al-Atrash,[4] Karen Dwyer,[4] Sanam Loghavi,[6] Rashmi Kanagal-Shamanna,[6] Xingzhi Song,[5] Jianhua Zhang,[5] Koichi Takahashi,[1] Hagop Kantarjian,[1] Guillermo Garcia-Manero,[1] and Simona Colla[1,8,*]

[1]Department of Leukemia, The University of Texas MD Anderson Cancer Center, Houston, TX, USA
[2]Department of Molecular, Cell and Developmental Biology, University of California Los Angeles, Los Angeles, CA, USA
[3]Department of Biostatistics, The University of Texas MD Anderson Cancer Center, Houston, TX, USA
[4]Department of Stem Cell Transplantation and Hematopoietic Biology and Malignancy, The University of Texas MD Anderson Cancer Center, Houston, TX, USA
[5]Department of Genomic Medicine, The University of Texas MD Anderson Cancer Center, Houston, TX, USA
[6]Department of Hematopathology, The University of Texas MD Anderson Cancer Center, Houston, TX, USA
[7]These authors contributed equally
[8]Lead contact
*Correspondence: scolla@mdanderson.org

https://doi.org/10.1016/j.xcrm.2024.101585

SUMMARY

RAS pathway mutations, which are present in 30% of patients with chronic myelomonocytic leukemia (CMML) at diagnosis, confer a high risk of resistance to and progression after hypomethylating agent (HMA) therapy, the current standard of care for the disease. Here, using single-cell, multi-omics technologies, we seek to dissect the biological mechanisms underlying the initiation and progression of *RAS* pathway-mutated CMML. We identify that *RAS* pathway mutations induce transcriptional reprogramming of hematopoietic stem and progenitor cells (HSPCs) and downstream monocytic populations in response to cell-intrinsic and -extrinsic inflammatory signaling that also impair the functions of immune cells. HSPCs expand at disease progression after therapy with HMA or the BCL2 inhibitor venetoclax and rely on the NF-κB pathway effector MCL1 to maintain survival. Our study has implications for the development of therapies to improve the survival of patients with *RAS* pathway-mutated CMML.

INTRODUCTION

Chronic myelomonocytic leukemia (CMML), a clonal disorder of mutant hematopoietic stem cells (HSCs),[1] is characterized by myelodysplastic and myeloproliferative bone marrow (BM) features,[2,3] and a high risk of progression to acute myeloid leukemia (AML).[4–6] Hypomethylating agent (HMA) therapy, the current standard of care for most patients with CMML,[7] can overcome CMML cells' aberrant proliferation and achieve improved outcomes in some patients. However, most patients only have transient responses to HMA therapy, owing to these agents' inability to effectively deplete HSCs and decrease tumor burden. CMML patients whose disease undergoes transformation to AML upon HMA therapy failure have dismal clinical outcomes.[8,9]

Despite advances in the genetic characterization of CMML, the development of alternative frontline treatments or more effective second-line therapies to improve the outcomes of CMML patients with high-risk biological features has been delayed because of an incomplete understanding of the ways in which different hematopoietic populations that persist throughout HMA therapy contribute to disease maintenance and progression.

Mutations in *RAS* pathway signaling genes (*BRAF*, *CBL*, *KRAS*, *NF1*, *NRAS*, and *PTPN11*) confer adverse biological features that increase the risk of disease progression and poor overall survival, particularly when they are concurrently present with loss-of-function mutations in the *ASXL* transcriptional regulator 1 gene, *ASXL1*.[10]

Herein, we used single-cell technology-based approaches to elucidate the biological and molecular landscape of *RAS* pathway-mutated CMML to guide the selection of future therapeutic interventions and achieve durable responses in CMML patients in whom blast progression (BP) occurs after failure to HMA therapy.

RESULTS

Mutations in *RAS* pathway signaling genes predict a high risk of CMML BP after HMA therapy failure

We first evaluated whether specific mutations predict a high risk of CMML BP in a cohort of 108 CMML patients who received

© 2024 The Authors. Published by Elsevier Inc.
This is an open access article under the CC BY-NC-ND license (http://creativecommons.org/licenses/by-nc-nd/4.0/).

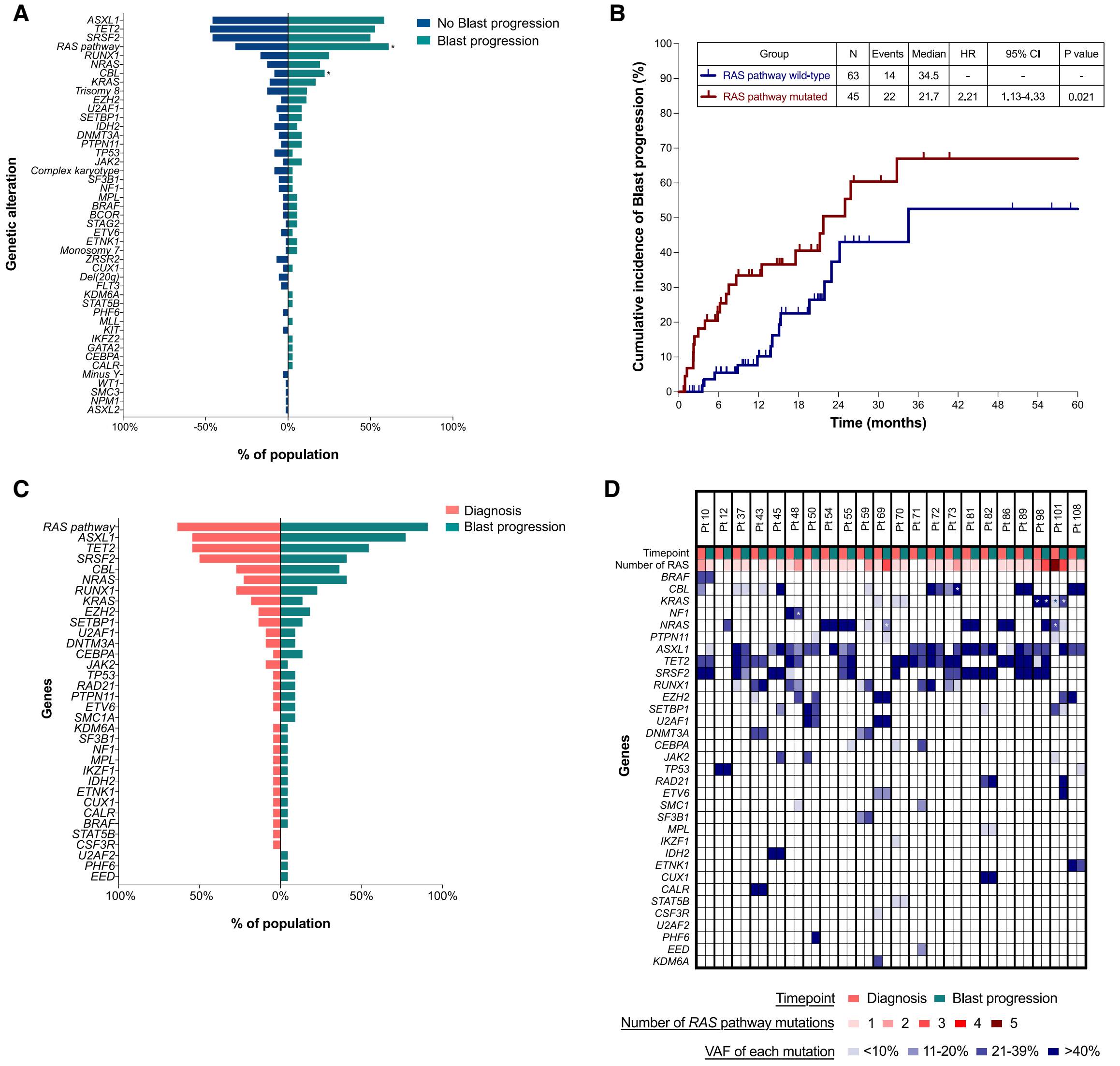

Group	N	Events	Median	HR	95% CI	P value
RAS pathway wild-type	63	14	34.5	-	-	-
RAS pathway mutated	45	22	21.7	2.21	1.13-4.33	0.021

Figure 1. Mutations in *RAS* pathway signaling genes predict a high risk of CMML BP after HMA therapy failure

(A) Bar chart showing the frequencies of detectable mutations and cytogenetic abnormalities among 108 CMML patients who received HMA therapy and whose disease progressed (green) or did not progress (blue). Asterisks indicate significantly different frequency changes (**p* < 0.05).

(B) Kaplan-Meier survival curves showing the cumulative incidence of BP after HMA therapy in previously untreated CMML patients with or without *RAS* pathway mutations. N, number; HR, hazard ratio; CI, confidence interval.

(C) Bar chart showing the overall frequencies of detectable mutations among 22 CMML patients whose disease progressed and in whom targeted sequencing was performed at the time of BP. Mutations at diagnosis and BP are indicated by pink and green, respectively. Paired samples were analyzed.

(D) Detected mutations and their variant allele frequencies (VAFs) in matched samples obtained at diagnosis and at the time of BP in the 22 CMML patients shown in (C). Columns represent the mutations and VAFs from sequential samples of individual CMML patients at diagnosis and BP. Patient identifiers are shown at the top of each column. Asterisks indicate the presence of multiple mutations in a particular gene. The numbers of *RAS* mutations are shown in red gradient; the VAFs of each mutation are shown in blue gradient.

HMA therapy (Table S1). After a median follow-up of 19 months (95% confidence interval [CI], 15.8–23.9 months), 57 patients experienced HMA therapy failure; 36 patients had BP at the time of therapy failure. Mutations in *RAS* pathway genes were significantly associated with BP (odds ratio = 3.35; 95% CI, 1.46–7.70; *p* = 0.004) (Figure 1A) and shorter time to BP (hazard ratio = 2.21; 95% CI, 1.13–4.33; *p* = 0.021) (Figure 1B). Similarly, logistic regression analysis showed that *RAS* pathway mutations were associated with a higher risk of BP (*p* = 0.01158) (Table S2). To assess whether BP was associated with mutations that were not detected at diagnosis or with the clonal expansion of pre-existing mutations, we sequenced BM cells isolated from samples collected at the time of BP after HMA failure from 22 of the 36 patients and compared the cells' genomic landscape with that of BM cells isolated at diagnosis (Figure 1C). Among 22 patients with BP, 14 (64%) had *RAS* pathway mutations at diagnosis,

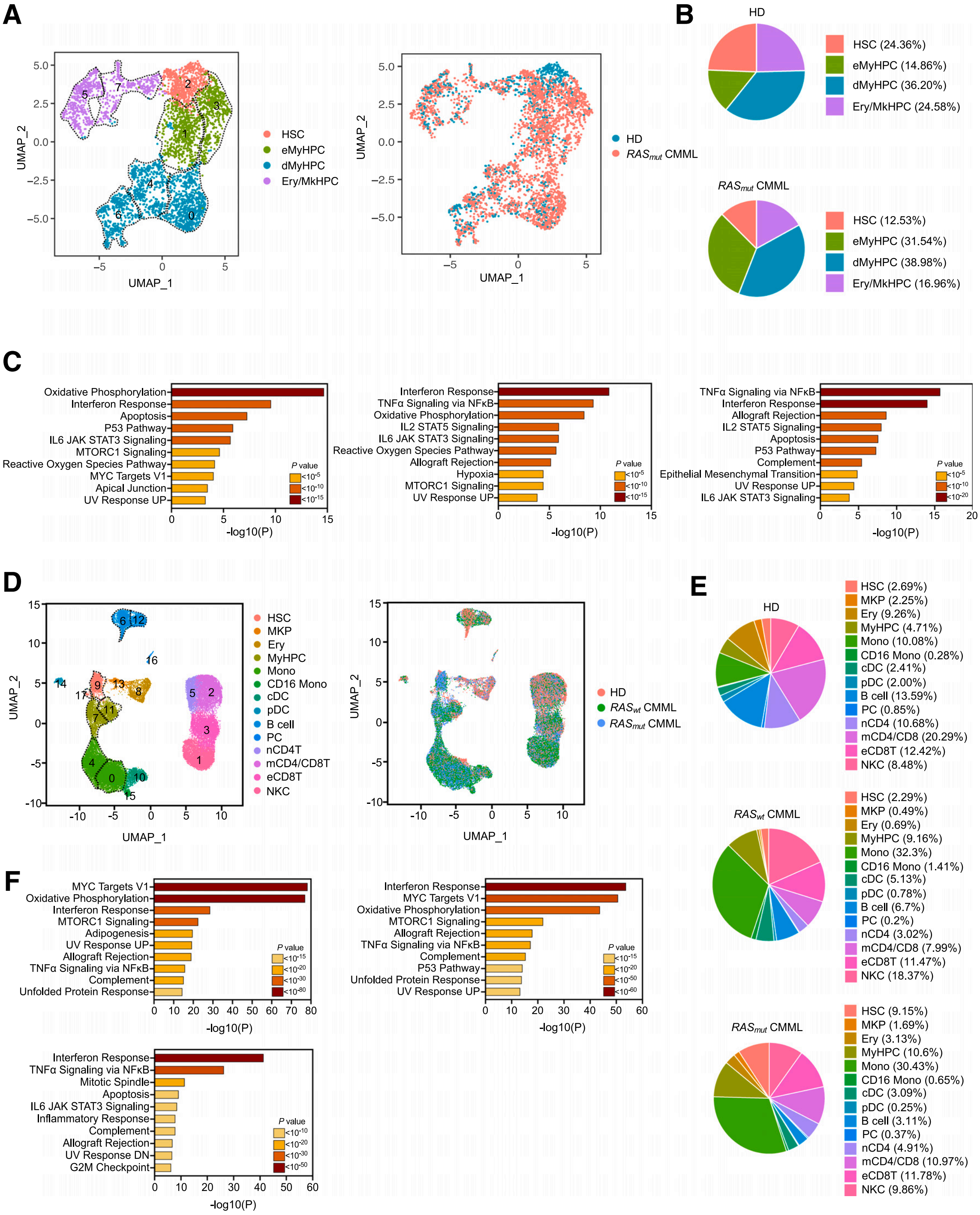

Figure 2. *RAS* pathway-mutated CMML cells activate cell-intrinsic and -extrinsic inflammatory networks

(A) UMAP of scRNA-seq data for pooled single Lin$^-$CD34$^+$ cells isolated from BM samples of two HDs (n = 895) and five *RAS* pathway mutant CMML patients (n = 3,161). Each dot represents one cell. Different colors represent the cluster cell-type identity (left) or sample origin (right). HSC, hematopoietic stem cells; eMyHPC, early myeloid progenitor cells; dMyHPC, differentiated myeloid progenitors; Ery/MkHPC, erythroid/megakaryocyte hematopoietic progenitor cells. Dashed lines indicate single clusters in each cell-type population.

(B) Distribution of HD (top) and *RAS* pathway mutant CMML (bottom) Lin$^-$CD34$^+$ cell types among the clusters shown in (A).

(C) Pathway enrichment analysis of the genes that were significantly upregulated in HSCs (left), eMyHPCs (middle), and dMyHPCs (right) from the five *RAS* pathway mutant CMML samples shown in (A) compared with those from HD samples (adjusted $p \leq 0.05$). The top 10 hallmark gene sets are shown.

(legend continued on next page)

and 20 (91%) had *RAS* pathway mutations at BP. Nine patients (41%) acquired newly detectable *RAS* pathway mutations at BP (4 patients had no detectable *RAS* pathway mutations at diagnosis, and 5 patients acquired other *RAS* pathway mutations). Of the 14 patients with *RAS* pathway-mutated CMML at diagnosis, 10 had BP without *RAS* pathway mutation-induced clonal evolution (Figure 1D).

These results were validated using single-cell DNA sequencing coupled with cell-surface immunophenotyping analysis of mononuclear cells (MNCs) isolated from sequential BM samples obtained at the time of diagnosis or BP from two representative *RAS* pathway-mutated CMML patients whose disease never responded to therapy (Figures S1A and S1B) or underwent clonal evolution after an initial response (Figures S2A and S2B). Taken together, these data demonstrate that patients with *RAS* pathway-mutated CMML have a high risk of BP at the time of HMA therapy failure. This observation has important clinical implications in light of our recent study showing that *RAS* pathway mutations also drive resistance to and/or BP following venetoclax-based second-line therapy.[11] These data underscore the urgent need to dissect the biological mechanisms of *RAS* pathway mutation-induced therapy resistance, as such an understanding could lead to the development of future therapeutic approaches to prevent or overcome disease progression.

RAS pathway mutations activate cell-intrinsic and -extrinsic inflammatory networks

To dissect the molecular mechanisms underlying the progression of *RAS* pathway-mutated CMML, we first evaluated the molecular determinants of disease initiation. We performed single-cell RNA sequencing (scRNA-seq) analysis of lineage-negative (Lin^-) $CD34^+$ hematopoietic stem and progenitor cells (HSPCs) isolated from five untreated *RAS* pathway mutant CMML patients and two age-matched healthy donors (HDs) (Table S3). This analysis identified eight cellular clusters driven by the differentiation profile of the cells (Figure 2A), which we defined based on the differential expression of validated lineage-specific transcriptional factors (TFs) and cellular markers[12,13] (Figure S3A; Table S4). Compared with HSPCs from HDs, Lin^-CD34^+ HSPCs from *RAS* pathway mutant CMML patients had a predominant myeloid differentiation route with higher frequencies of early myeloid hematopoietic progenitor cells (eMyHPCs) (clusters 1 and 3, characterized by the high expression of *CD34*, *BTF3*, and *CEBPA* but low expression of *CD38*) and more differentiated MyHPCs (dMyHPCs) (clusters 0, 4, and 6, marked by the expression of *CEBPD* and/or *CEBPA*, as well as that of *MPO*) at the expense of more primitive HSCs (cluster 2, marked by the high expression of *MLLT3*, *MEG3*, and *CLEC9A*), and erythroid/megakaryocyte (Ery/Mk) HPCs (clusters 5 and 7, marked by the expression of *KLF1*, *GATA1*, and *GATA2*) (Figure 2B). Differential expression analysis revealed that genes upregulated in *RAS* pathway mutant CMML HSCs compared with HD HSCs were mainly involved in oxidative phosphorylation, interferon (IFN) response, and apoptosis (Figures 2C and S3B). Similar results were observed in eMyHPCs and dMyHPCs (Figure 2C).

To evaluate the contribution of downstream myelo/monocytic (My/Mo) populations to disease maintenance, we performed scRNA-seq analysis of BM MNCs isolated from three HDs, and five untreated *RAS* pathway mutant CMML samples. To dissect the specific role of *RAS* pathway mutations in disease initiation, we also included BM MNCs from three untreated *RAS* pathway wild-type CMML samples. This analysis identified 18 cellular clusters inclusive of all major BM cell types that we defined based on the expression of lineage-specific TFs and cellular markers and using the single-cell transcriptome to protein prediction with deep neural network pipeline[14,15] (Figures 2D and S3C; Table S5). Consistent with the predominant myeloid differentiation bias of CMML HSPCs, differential analysis of BM cell lineage composition revealed that the monocyte population (clusters 0 and 4) increased in BM CMML samples compared with that in BM HD samples, regardless of the presence of *RAS* pathway mutations (Figure 2E).

However, although CMML monocytes from *RAS* pathway wild-type CMML underwent transcriptional reprogramming compared with those from HDs, *RAS* pathway mutant monocytes had significantly enhanced upregulation of IFN and NF-κB signaling-mediated inflammatory responses compared with *RAS* pathway wild-type monocytes (Figures 2F and S4A).

Inflammatory networks modulate the immune microenvironment and contribute to immune escape.[16] To assess whether CMML monocytes directly suppress the immune response and whether *RAS* pathway mutations modulate such interactions, we dissected the intercellular crosstalk and communication networks between CMML cells and all other BM cells. We inferred cell-to-cell communications from the combined expression of multi-subunit ligand-receptor complexes using CellPhoneDB, a repository of ligands and receptors and their interactions.[17] After generating a homeostatic interactome of BM MNCs from HDs, we analyzed the cellular communication networks that were upregulated in *RAS* pathway wild-type and mutant CMML BM samples (Figure S4B; Table S6). Compared with HD MNCs, *RAS* pathway mutant CMML MNCs had significantly more ligand-receptor interactions

(D) UMAP of scRNA-seq data for pooled single MNCs isolated from BM samples of three HDs ($n = 12{,}836$), three *RAS* pathway wild-type (RAS_{wt}) ($n = 16{,}038$), and five *RAS* pathway mutant (RAS_{mut}) ($n = 12{,}234$) CMML patients. Each dot represents one cell. Different colors represent the cluster cell-type identity (left) or sample origin (right). HSC, hematopoietic stem cells; MKP, megakaryocyte precursors; Ery, erythroid precursors; MyHPC, myeloid hematopoietic progenitor cells; Mono, monocytes; CD16 Mono, non-classical $CD16^+$ monocytes; cDC, classical dendritic cells; pDC, plasmacytoid dendritic cells; B cell, B lymphocytes; PC, plasma cells; nCD4T, naive $CD4^+$ T cells; mCD4/CD8, memory $CD4^+$ and $CD8^+$ T cells; eCD8T, effector $CD8^+$ T cells; NKC, natural killer cells. Dashed lines indicate single clusters in each cell-type population.

(E) Distribution of HD (top), and *RAS* pathway wild-type (RAS_{wt}) (middle) or mutant (RAS_{mut}) CMML (bottom) BM MNC populations among the clusters shown in (D).

(F) Pathway enrichment analysis of the genes that were significantly upregulated in *RAS* pathway wild-type (top left) or mutant (top right) CMML monocyte clusters compared with those in HD and *RAS* pathway mutant monocyte clusters compared with those in *RAS* pathway wild-type monocyte clusters (bottom left) (adjusted $p \leq 0.05$). The top 10 hallmark gene sets are shown.

involving monocytes, classical dendritic cells (cDCs), plasmacytoid DCs (pDCs), MyHPCs, effector CD8$^+$ T (eCD8T) cells, and natural killer (NK) cells (Figure S4B). Monocytes, cDCs, and immune populations from patients with *RAS* pathway mutant CMML gained significantly more ligand-to-receptor interactions compared with those without *RAS* pathway mutations (Figure S4B). Specifically, expression levels of chemokine genes (*CCL3* and *CCL3L1*) and cytokine genes (*IL1B*, *TNFSF10*, *MIF*, and *HGF*) involved in inflammatory signaling and NF-κB-mediated cell survival were significantly increased in CMML monocytes, cDCs, pDCs, and MyHPCs, and enriched in patients with *RAS* pathway mutations (Figure S4C). Monocytes and cDCs from patients with *RAS* pathway mutations expressed higher levels of the receptors of these ligands (*CCR1*, *CCR5*, *CD74*, and *TNFRSF10B*), which suggests that an aberrant feedback loop among different cell types preferentially contributes to CMML maintenance in *RAS* pathway mutant CMML. Together, these data are consistent with previous findings showing that, in other cancers, NF-κB signaling activation is essential for *RAS* pathway mutation-induced tumorigenesis.[18–21]

CMML monocytes, pDCs, and cDCs also gained cell-to-cell interactions with NK and eCD8T cells. Interactions involving the HLA-E-KLRC1/2, CDH1-KLRG1, LGALS9-HAVCR2, and TGFB1-TGBR1/3 ligand-receptor pairs (known to inhibit the immune cell functions[22–29]) were the most common (Figure S4C; Table S6). To evaluate whether CMML BM monocytes and immune cells spatially co-localized, we performed multiplex immunofluorescence analysis of BM biopsy sections obtained from CMML patients ($n = 4$) at the time of diagnosis. This analysis revealed that BM monocytes (CD14$^+$CD68$^-$ cells) resided within a median of 19.73 μm (95% CI, 12.75–32.25 μm) from CD8$^+$ T cells and 22.62 μm (95% CI, 15.73–32.17 μm) from NK cells (CD3$^-$CD56$^+$ cells; Figures S5A and S5B), which suggests that these cell populations interact with each other. Accordingly, both CMML NK cells (cluster 1) and eCD8T cells (cluster 3) had increased expression levels of immune checkpoint genes associated with these cells' exhaustion (e.g., *KLRG1*, *KLRC1*, *TIGIT*, *LAG3*, *CD244*, *B3GAT1*, and *CD160*) compared with those from HDs (Figure S5C).[30–32] To further characterize the functional state of CD8$^+$ T and NK cells in CMML, we evaluated the expression of activation markers on these cells after antigen exposure. After co-culture with K562 AML cells, the frequencies of IFN-γ$^+$ CD8$^+$ T cells and activated CD16$^+$ NK cells were significantly lower in *RAS* pathway mutant CMML but not in *RAS* pathway wild-type CMML, compared with those in HDs (Figure S5D). In addition, IFN-γ$^+$ CD8$^+$ T cells and NK cells from patients with *RAS* pathway mutant CMML, but not those from *RAS* pathway wild-type CMML, had significantly lower IFN-γ and perforin expression levels, respectively (Figure S5D).

Taken together, these data suggest that CMML HSPCs and downstream My/Mo cells undergo significant transcriptional rewiring and that *RAS* pathway mutations enhance the activation of cell-intrinsic and -extrinsic inflammatory networks in CMML monocyte populations to maintain cell proliferation and suppress the immune microenvironment, thus enabling immune escape and clonal expansion.

RAS pathway-mutated HSCs upregulate NF-κB transcriptional programs and drive CMML BP after HMA therapy failure

To evaluate the cellular and molecular dynamics of CMML progression, we performed scRNA-seq analysis of Lin$^-$CD34$^+$ HSPCs isolated from BM samples sequentially obtained from five *RAS* pathway mutant CMML patients at diagnosis and BP (Figures 3A and S6A; Table S7). HSPCs isolated from BM samples obtained at BP maintained aberrant differentiation toward the My/Mo lineage (Figure 3B) and had upregulated genes belonging to the NF-κB signaling pathway (Figure 3C). Importantly, *MCL1*, an anti-apoptotic member of the BCL2 family and a downstream effector of the NF-κB pathway, was significantly upregulated in HSCs (cluster 6) and eMyHPCs (clusters 0 and 1) at BP compared with those at diagnosis (Figures S6B and S6C; Table S8).

To evaluate whether HSPCs' transcriptional changes at BP resulted from epigenetic reprogramming in the more primitive HSCs, we performed single-cell assays for transposase-accessible chromatin with high-throughput sequencing (scATAC-seq) to profile the chromatin accessibility landscape in Lin$^-$CD34$^+$ HSPCs isolated from BM samples sequentially obtained from three *RAS* pathway mutant CMML patients at diagnosis or BP. Our analysis identified five clusters with distinct TF binding motif enrichment in the open chromatin regions (Figures 3D and S6D; Table S9). MyHPCs (clusters 1 and 2) were characterized by open chromatin regions in the binding motifs of the myeloid TFs *SPI1B* and *CEBPA* and TFs belonging to the *FOS* and *JUN* families. HSCs (clusters 0 and 4) had the highest activities of TFs involved in stemness maintenance, such as *HLF* and TFs belonging to the nuclear retinoid receptor and EGR families. Ery/MkHPCs (cluster 3) were characterized by open chromatin regions in binding motifs for GATA TFs.

Consistent with our transcriptomic data, HSCs at BP had increased open chromatin peaks at the promoters of genes involved in NF-κB pathway activation and inflammatory response pathways (Figure 3E), including *MCL1* (Figure S6E; Table S10). HSCs also showed increased open chromatin peaks of genes involved in NF-κB pathway activation and inflammatory response pathways at the genes' distal elements, which define cell identity and differentiation trajectories more precisely than promoter regions do[33] (Figures 3F and S6F).

Taken together, these data suggest that *RAS* pathway-mutated CMML HSCs exacerbate the activation of inflammatory and NF-κB pathway transcriptional programs and promote transcriptional upregulation of NF-κB signaling-mediated anti-apoptotic pathways to maintain survival at BP after HMA failure.

RAS pathway-mutated CMML cells rely on *MCL1* overexpression to maintain their survival at BP

To elucidate whether MyHPCs' transcriptional and epigenetic reprogramming drives BP, we performed scRNA-seq analysis of MNCs isolated from sequential *RAS* pathway-mutated CMML BM samples obtained from six CMML patients at diagnosis and BP (Figures 4A and S7A; Table S11). MNCs at BP had a significantly higher frequency of CD34$^+$ MyHPCs (22.5% vs. 2.8%, respectively; clusters 7, 8, and 14) compared with those at diagnosis (Figures 4B and S7B). These results were confirmed

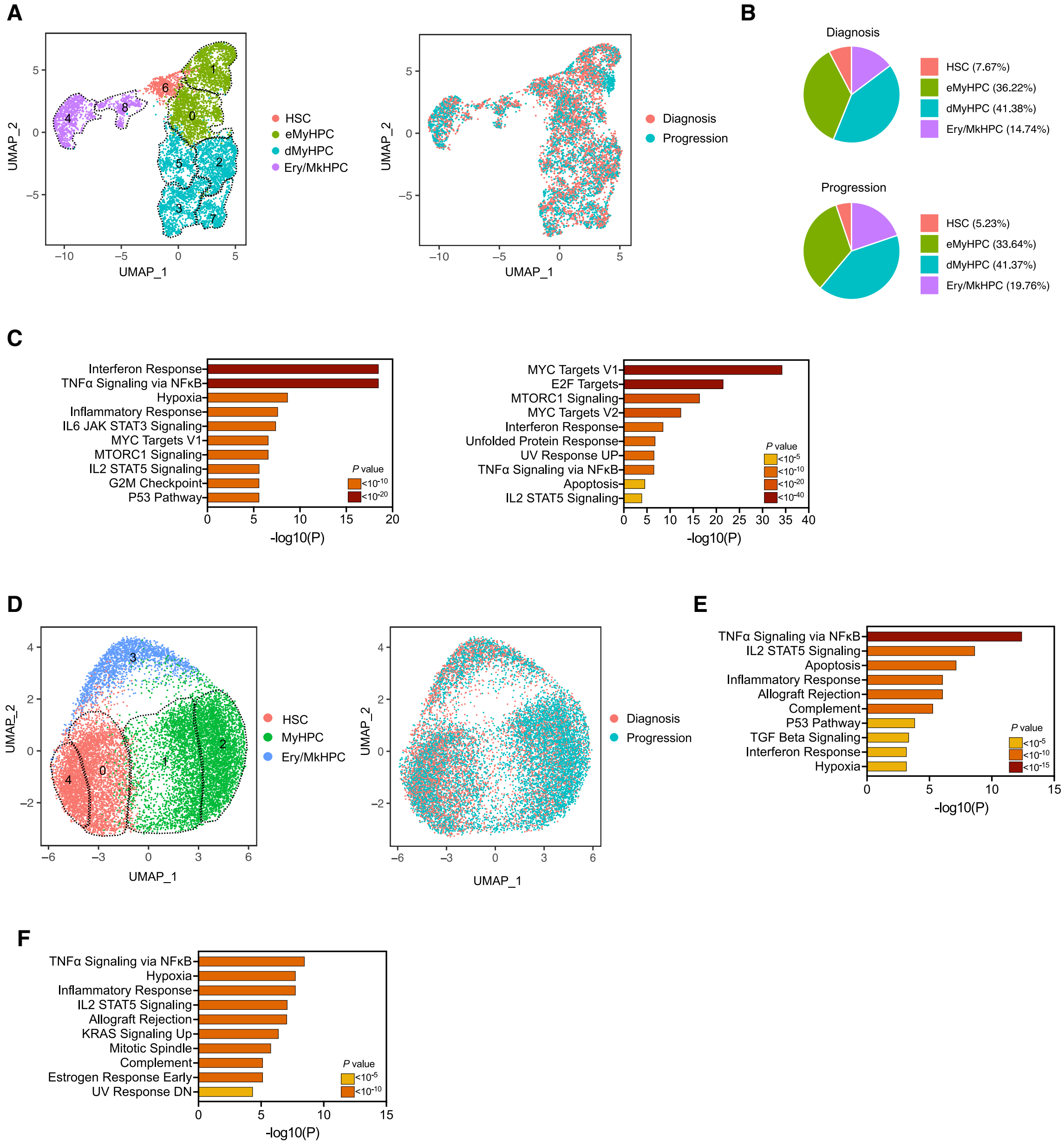

Figure 3. ***RAS*** **pathway-mutated HSCs undergo epigenetic reprogramming and drive CMML BP after HMA therapy failure**

(A) UMAP of scRNA-seq data for pooled single $\text{Lin}^{-}\text{CD34}^{+}$ cells isolated from BM samples of five *RAS* pathway mutant CMML patients at diagnosis ($n = 1{,}840$) and at BP after HMA therapy failure ($n = 1{,}711$). Each dot represents one cell. Different colors represent the cluster cell-type identity (left) or sample origin (right). HSC, hematopoietic stem cells; eMyHPC, early myeloid hematopoietic progenitor cells; dMyHPC, differentiated myeloid hematopoietic progenitor cells; Ery/MkHPC, erythroid/megakaryocyte hematopoietic progenitor cells. Dashed lines indicate single clusters in each cell-type population.

(B) Distribution of $\text{Lin}^{-}\text{CD34}^{+}$ cell types at diagnosis (top) and BP (bottom) among the clusters shown in (A).

(C) Pathway enrichment analysis of the genes that were significantly upregulated in HSCs (left) and dMyHPCs (right) at the time of BP after HMA therapy failure compared with those at diagnosis (adjusted $p \leq 0.05$). The top 10 hallmark gene sets are shown.

(D) UMAP of scATAC-seq data for pooled $\text{Lin}^{-}\text{CD34}^{+}$ cells isolated from BM samples obtained from three *RAS* pathway mutant CMML patients at diagnosis ($n = 5{,}066$) and at BP after HMA therapy failure ($n = 8{,}603$). Each dot represents one cell. Different colors represent the cluster identity (left) or sample of origin (right). HSC, hematopoietic stem cells; MyHPC, myeloid progenitor cells; Ery/MkHPC, erythroid/megakaryocyte hematopoietic progenitor cells.

(E) Pathway enrichment analysis of genes whose promoters were enriched in open chromatin regions in HSCs (clusters 0 and 4, shown in D) at the time of BP as compared with those at diagnosis ($p \leq 10^{-4}$). The top 10 hallmark gene sets are shown.

(F) Pathway enrichment analysis of genes whose distal elements were enriched in open chromatin regions in HSCs (clusters 0 and 4, shown in D) at the time of BP as compared with those at diagnosis (adjusted $p \leq 0.05$). The top 10 hallmark gene sets are shown.

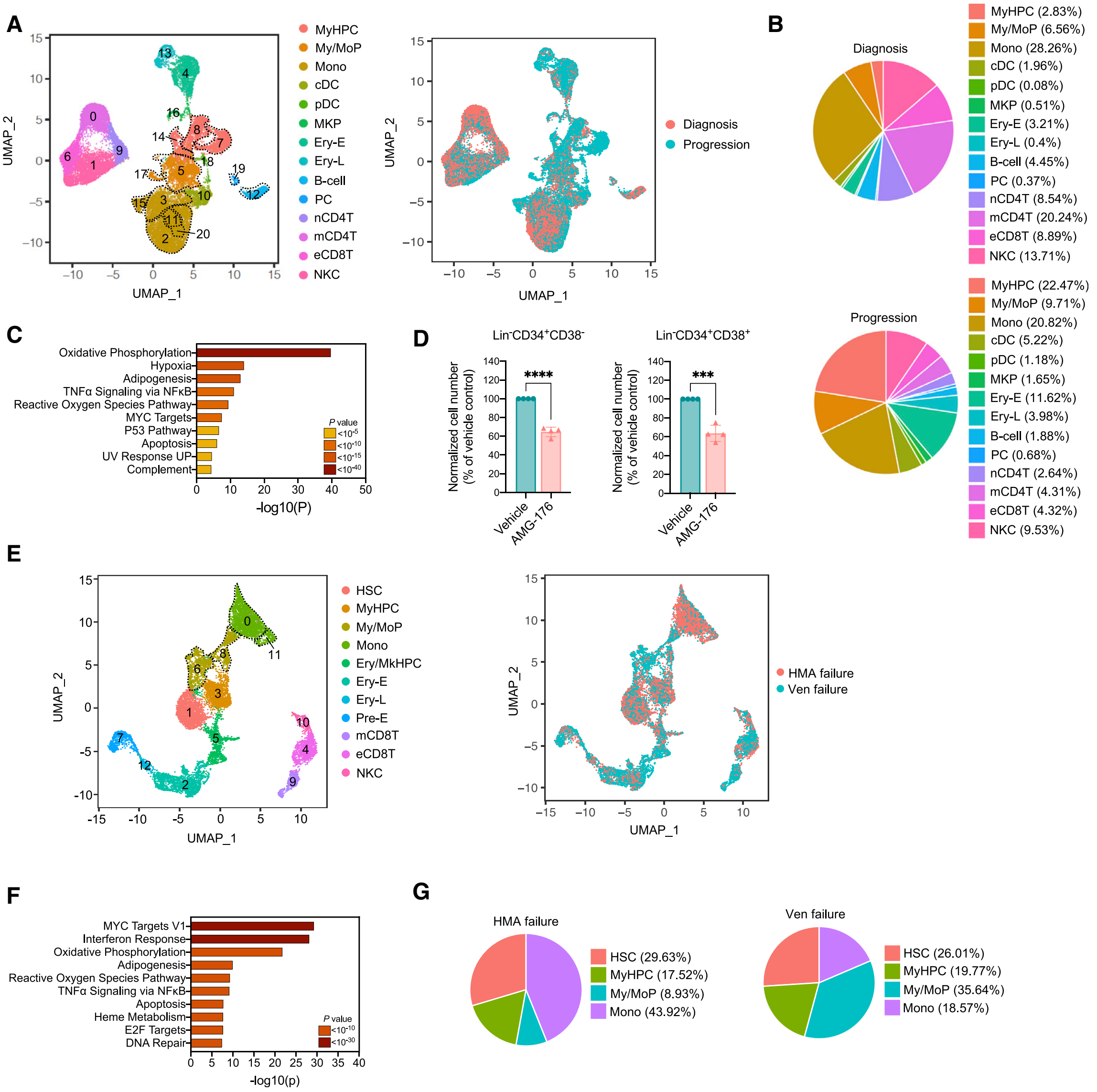

Figure 4. *RAS* pathway-mutated CMML cells rely on *MCL1* overexpression to maintain their survival at BP

(A) UMAP of scRNA-seq data for pooled single MNCs isolated from BM samples of six *RAS* pathway mutant CMML patients at diagnosis ($n = 16{,}372$) and at BP after HMA therapy failure ($n = 19{,}541$). Each dot represents one cell. Different colors represent the cluster cell-type identity (left) or sample of origin (right). MyHPC, myeloid hematopoietic progenitor cells; My/MoP, myelo/monocytic progenitors; Mono, monocytes; cDC, classical dendritic cells; pDC, plasmacytoid dendritic cells; MKP, megakaryocyte precursors; Ery-E, early erythroid precursors; Ery-L, late erythroid precursors; B cell, B lymphocytes; PC, plasma cells; nCD4T, naive CD4$^+$ T cells; mCD4T, memory CD4$^+$ T cells; eCD8T, effector CD8$^+$ T cells; NKC, natural killer cells. Dashed lines indicate single clusters in each cell-type population.

(B) Distribution of MNC populations at diagnosis (top) and progression (bottom) among the clusters shown in (A).

(C) Pathway enrichment analysis of the genes that were significantly upregulated in the monocytic populations (clusters 2, 3, 11, 15, and 20) shown in (A) at the time of BP after HMA therapy failure compared with those at diagnosis (adjusted $p \leq 0.05$). The top 10 hallmark gene sets are shown.

(D) Numbers of live Lin$^-$CD34$^+$CD38$^-$ HSCs and Lin$^-$CD34$^+$CD38$^+$ MyHPCs from CMML patients with BP after treatment with vehicle or AMG-176 ($n = 4$, 20 nM) for 48 h. Lines represent means ± SD. Statistical significance was calculated using a two-tailed Student's t test (***$p < 0.001$, ****$p < 0.0001$).

(E) UMAP of scRNA-seq data for pooled single MNCs isolated from BM samples obtained from a representative CMML patient at the time of BP after HMA therapy failure ($n = 6{,}209$) and subsequent failure to venetoclax-based therapy ($n = 6{,}795$). Each dot represents one cell. Different colors represent the cluster cell-type identity (left) or the sample of origin (right). HSC, hematopoietic stem cells; MyHPC, myeloid hematopoietic progenitor cells; My/MoP, myelo/monocytic progenitors; Mono, monocytes; Ery/MkHPC, erythroid/megakaryocytic hematopoietic progenitor cells; Ery-E, early erythroid precursors; Ery-L, late erythroid precursors; Pre-E, pre-erythrocytes; mCD8T, memory CD8$^+$ T cells; eCD8T, effector CD8$^+$ T cells; NKC, natural killer cells.

(F) Pathway enrichment analysis of the genes that were significantly upregulated in MyHPCs at the time of venetoclax failure compared with those at the time of BP after HMA therapy failure (adjusted $p \leq 0.05$). The top 10 hallmark gene sets are shown.

(G) Distribution of myeloid cell types among the myeloid compartments at BP after HMA therapy failure (left) and venetoclax-based therapy failure (right).

by flow cytometry analysis of Lin$^-$CD34$^+$ cells in 70% of the patients (Figure S7C), which suggests that BP after HMA therapy is mostly driven by the expansion of the HSPC compartment. Consistent with our results in the Lin$^-$CD34$^+$ compartment, differential expression analysis confirmed that MyHPCs at BP had upregulated genes involved in TNF-α-mediated NF-κB activation (Figure S7D), including *MCL1* (Figures S7E and S7F; Table S12). The upregulation of these genes was maintained in downstream My/Mo progenitors (My/MoPs; clusters 5 and 17) and was significantly increased in the monocytic populations (clusters 2, 3, 11, 15, and 20) (Figures 4C and S7G; Table S12). Consistent with these transcriptomic results, CD34$^+$ BM cells from patients with *RAS* pathway mutant CMML at BP (n = 2) had higher MCL1 protein expression than did cells from patients at diagnosis (n = 3; Figure S7H).

MNCs at BP exacerbated the cellular communication networks between cDCs, MyHPCs, My/MoPs, pDCs, monocytes, and eCD8T cells, compared with MNCs at baseline. Exacerbation of the cellular communication networks mainly occurred through immune-suppressive interactions between the LGALS9-HAVCR2 ligand-receptor pair, as well as increased CCL3/CCR1 and HGF/CD44 interactions between monocytes, MyMoPs and MyHPCs (Figures S8A and S8B; Table S13).

To determine whether *MCL1* upregulation was a hallmark of BP in *RAS* pathway mutant CMML or a general mechanism of treatment resistance and progression in CMML, we performed scRNA-seq analysis of BM MNCs isolated from *RAS* pathway wild-type CMML samples at diagnosis (n = 3) and BP after HMA failure (n = 3) (Figures S9A and S9B; Table S14). *RAS* pathway wild-type BM MNCs at progression had a higher frequency of MyHPCs compared with those at diagnosis (8.1% vs. 3.9%, respectively; cluster 7; Figure S9C). MyHPCs at BP upregulated genes involved in TNF-α-mediated NF-κB activation but not *MCL1* (Figures S9D and S9E; Table S15). Similar data were also observed in downstream My/MoPs and monocytes (Figure S9D; Table S15). Consistent with these findings, CD34$^+$ BM cells from patients with *RAS* pathway wild-type CMML at diagnosis (n = 3) and BP (n = 3) had similar MCL1 protein expression levels (Figure S7H).

Together, these data suggest that only *RAS* pathway-mutated CMML MyHPCs and monocytes rely on *MCL1*-driven anti-apoptotic pathways to maintain survival and expand after therapy failure. To test this hypothesis, we treated Lin$^-$CD34$^+$ HSPCs isolated from the BM of patients with *RAS* pathway-mutated CMML with the MCL1 inhibitor AMG-176[34] (at a dose that did not deplete Lin$^-$CD34$^+$CD38$^-$ or Lin$^-$CD34$^+$CD38$^+$ HSPCs isolated from the BM of HDs in co-culture system with mesenchymal stromal cells; Figure S10A). AMG-176 significantly decreased the numbers of Lin$^-$CD34$^+$CD38$^-$ and Lin$^-$CD34$^+$CD38$^+$ HSPCs isolated from BM samples obtained from patients with *RAS* pathway-mutated CMML at BP (Figure 4D). AMG-176 did not significantly affect the survival of HSPCs isolated from BM samples obtained from patients at diagnosis (Figure S10B), which confirms that CMML HSPCs maintain an intact apoptotic program at disease initiation. Consistent with our scRNA-seq analysis showing that *MCL1* was not upregulated in *RAS* pathway wild-type HSPCs, the treatment with AMG-176 did not deplete *RAS* pathway wild-type HSPCs at the time of BP after HMA failure (Figure S10C).

Importantly, *BCL2* was not overexpressed in either *RAS* pathway mutant CMML HSPCs or downstream My/Mo populations at BP after HMA therapy failure (Figure S10D). *BCL2* expression was significantly downregulated at progression in MyHPCs and My/MoPs from CMML patients without detectable *RAS* pathway mutations at the time of BP (Figure S10E). These findings are consistent with our previous clinical observation that CMML patients in whom HMA therapy has failed do not benefit from second-line therapy with venetoclax.[11] Indeed, scRNA-seq analysis of MNCs isolated from sequential BM samples obtained from one representative *RAS* pathway mutant CMML patient whose disease progressed after HMA therapy failure and did not respond to venetoclax therapy (Figures 4E and S10F; Table S16) revealed that MyHPCs further exacerbate the expression of genes involved in TNF-α-mediated NF-κB pathway activation (Figure 4F), including *MCL1* (Figure S10G). Venetoclax failure was associated with a significant expansion of downstream My/MoPs in the myeloid compartment (Figure 4G) and these cells' high expression of *MCL1* (Figure S10G).

Taken together, our findings suggest that venetoclax therapy cannot overcome HMA failure-induced transcriptional reprogramming in My/MoPs and provide a rationale for targeting effectors of the NF-κB signaling pathway, such as MCL1, in patients with *RAS* pathway mutant CMML to improve the dismal outcome of CMML patients whose disease is resistant to available therapies.

DISCUSSION

Whereas the dissection of the molecular landscape of CMML initiation and progression has significantly advanced our understanding of the pathogenesis of CMML,[1,35–38] the development of more effective therapeutic approaches to improve patient survival has been delayed by our limited understanding of the ways in which genetic alterations affect distinct transcriptional states of My/Mo differentiation.

Mutations in *RAS* pathway genes, which are present in 30% of CMML patients,[38] are enriched during disease progression in up to 90% of the cases and predict a higher risk of and a shorter time to relapse after HMA and venetoclax therapy.[39] Currently, there are no other therapies that improve the survival duration of patients with *RAS* pathway-mutated CMML.

Using single-cell multi-omics technologies, we sought to dissect the biological mechanisms behind *RAS* pathway mutation-induced CMML evolution with the overall goal of identifying cellular vulnerabilities that could be therapeutically targeted to halt disease progression. We found that, at disease initiation, *RAS* pathway mutant CMML HSPCs significantly upregulated genes involved in the cell-intrinsic IFN signaling pathway such as *IRF1*, IRF7, *IRF9*, *IFI44*, *IFI44L*, *IFIH1*, *IFIT3*, or *STAT2* that drive these cells' differentiation toward the My/Mo lineage while maintaining an intact apoptotic program. Consistent with this observation and prior studies showing that *KRAS* or *NRAS* mutations directly activate intrinsic IFN-stimulated genes,[40] IFN signaling activation in HSPCs was not associated with IFN receptor (*IFNAR1*, *IFNAR2*, *IFNGR1*, or *IFNG2*) or ligand (*IFNG* or

IFNA) overexpression. In addition, this inflammatory reprogramming was exacerbated in downstream *RAS* pathway mutant monocyte populations, which expressed high levels of cytokines and cell surface receptors involved in NF-κB pathway activation and immune evasion. These results suggest that disease initiation and maintenance, as a result of *RAS* pathway mutations, rely on the activation of both cell-intrinsic and -extrinsic inflammatory networks in distinct cell populations and provide a rationale for using inhibitors of NF-κB-associated inflammatory signaling cascades as a frontline treatment for patients with *RAS* pathway-mutated CMML. These findings, which are consistent with previous studies showing the role of inflammatory cell populations in myeloid malignancies,[41,42] have significant implications since several inflammation-targeting therapies that are currently in clinical development have shown great potential to treat patients with myeloid malignancies.[43–45]

Consistent with the long-standing observation that inhibition of apoptosis contributes to therapy resistance and cancer progression, we found that *RAS* pathway mutant CMML HSPCs isolated from BM samples at the time of BP depended on MCL1, an anti-apoptotic downstream effector of the NF-κB pathway, to maintain their survival and undergo clonal expansion. Consistent with this observation, we had demonstrated previously that TNF-α-mediated NF-κB pathway activation represents a cell-intrinsic adaptive mechanism to overcome cell death in response to therapeutic pressure.[46] In addition, our findings align with prior data demonstrating that *RAS* mutations can directly induce NF-κB hyperactivation.[21,47] Notably, targeting MCL1 activity with the small molecule AMG-176 only significantly depleted HSPCs from *RAS* mutant CMML but not those from *RAS* wild-type CMML, a finding that supports the selective use of MCL1 inhibitors to treat patients with *RAS* pathway mutant CMML in whom BP occurs at the time of HMA therapy failure. These results are consistent with previous findings showing that CMML monocytes rely on MCL1, but not BCL2, for survival,[48] and that *NRAS*-mutant monocytic subclones that emerge at AML relapse depend on MCL1, not BCL2, for energy production.[49] Consistent with this observation, our scRNA-seq analysis of BM MNCs from one representative patient with venetoclax-resistant disease confirmed that BCL2 inhibition cannot overcome the activation of NF-κB pathway-mediated inflammatory and survival mechanisms in HSPCs and downstream My/Mo populations.

In conclusion, this study highlights the importance of dissecting how specific genetic drivers affect the cell-of-origin in cancer to gain mechanistic insights into therapy failure and, thereby, develop selective therapeutic approaches to halt disease progression. Given that the *RAS* pathway mutation-induced reprogramming of CMML cells is a multi-step process that affects multiple biological signaling pathways (e.g., inflammation, apoptosis, and immune escape) in distinct BM cell types, our findings also suggest that only combination therapies that simultaneously target these pathways could effectively overcome disease progression and prolong the survival of patients whose disease is resistant to current therapeutic approaches.

Limitations of the study

In this study, we used 3′ RNA-seq by 10X Genomics, which evaluates RNA transcript expression levels for individual genes at the single-cell level but does not capture the entire RNA sequence, hence not allowing inference of the complete cDNA sequence and somatic mutation detection. Therefore, we were not able to correlate transcriptome to *RAS* pathway mutation status with single-cell resolution in all sequenced cases. Although we attempted to mitigate this intrinsic limitation to our sequencing technique by selecting samples with high *RAS* pathway mutant variant allele frequencies (VAFs), future studies will require the use of alternative single-cell sequencing technologies able to simultaneously capture genotype and transcriptome at the single-cell level to invariably characterize the specific features of *RAS* pathway mutant vs. wild-type cells. In an attempt to mitigate the impact of such a limitation in our identification of MCL1 upregulation as a preferential *RAS* mutant cell survival mechanism, we confirmed MCL1 upregulation at the protein level by evaluating *RAS* pathway mutant samples with high VAFs. In addition, although we were able to confirm the selective sensitivity of *RAS* pathway mutant $\text{Lin}^{-}\text{CD34}^{+}$ cells to MCL1 inhibition at the time of progression after HMA therapy failure, there are inherent limitations to the extent to which these studies can capture the *in vivo* effects of MCL1 inhibition and how this could affect distinct cell types and functionalities. Finally, although we validated our transcriptomic findings related to cell-cell communication networks between key BM populations with multiplex immunofluorescence and immunophenotypic immune cell characterization, future studies will require deeper investigation and validation of these interactions.

STAR★METHODS

Detailed methods are provided in the online version of this paper and include the following:

- KEY RESOURCES TABLE
- RESOURCE AVAILABILITY
  - ○ Lead contact
  - ○ Materials availability
  - ○ Data and code availability
- EXPERIMENTAL MODEL AND STUDY PARTICIPANT DETAILS
  - ○ Primary human samples
- METHOD DETAILS
  - ○ Clinical data analysis
  - ○ Flow cytometry analysis and fluorescence-activated cell sorting (FACS)
  - ○ Multiplex imaging assay
  - ○ Western blot
  - ○ T cell and NK cell cytokine secretion assays
  - ○ scRNA-seq analysis and bioinformatic pipeline
  - ○ scATAC-seq analysis and bioinformatic pipeline
  - ○ scDNA and protein-seq analysis
  - ○ Primary cell culture assays
- QUANTIFICATION AND STATISTICAL ANALYSIS

SUPPLEMENTAL INFORMATION

Supplemental information can be found online at https://doi.org/10.1016/j.xcrm.2024.101585.

ACKNOWLEDGMENTS

This work was supported by philanthropic contributions to MD Anderson's AML/MDS Moon Shot, the Edward P. Evans Foundation, and the National

Institutes of Health through a Leukemia SPORE grant awarded to the MD Anderson Cancer Center (P50 CA100632). J.J.R.-S. is a recipient of the Odyssey Fellowship awarded by the MD Anderson Cancer Center. This work used MD Anderson's South Campus Flow Cytometry & Cellular Imaging Facility and the Advanced Technology Genomics Core at the MD Anderson Cancer Center; the facilities are supported in part by the National Institutes of Health (National Cancer Institute) through MD Anderson's Cancer Center Support Grant (P30 CA16672). The authors thank Joseph Munch for assistance with manuscript editing. The authors give thanks for the technical support of the following Translational Molecular Pathology-Immunoprofiling Laboratory members: Daniela E. Duenas, Mario L. Marques-Piubelli, Mei Jiang, Beatriz Sanchez-Espidion, Salome McAllen, and Jianling Zhou. The graphical abstract was created with Biorender.com.

AUTHOR CONTRIBUTIONS

G.M.-B. and S.C. designed the research. N.T., J.J.R.-S., I.G.-G., H.Y., V.A., and B.W. performed the experiments. F.M. analyzed scRNA and scATAC-seq data. S.L., R.K.-S., X.S., and J.Z. analyzed targeted DNA sequencing data. Y.J.K., T.T., and K.T. performed scDNA and protein-seq experiments. K.D. analyzed the flow cytometry data. G.M.-B. and J.J.R.-S. identified the clinical samples included in the study. G.M.-B. and F.D. analyzed the clinical data. G.A.-A. provided the HD samples. H.K. and G.G.-M. made critical intellectual contributions throughout the study. G.M.-B. and S.C. wrote the manuscript.

DECLARATION OF INTERESTS

G.M.-B. declares research support from Rigel Pharmaceuticals, IFM Therapeutics, and Takeda Oncology. K.T. declares support from Symbio Pharmaceuticals, Novartis, Celgene/BMS, and GSK, and honoraria from Mission Bio and Illumina. H.K. declares research support from and an advisory role at Actinium and research support from AbbVie, Agio, Amgen, Ariad, Astex, Bristol Myers Squibb, Cyclacel, Daiichi-Sankyo, Immunogen, Jazz Pharma, Novartis, and Pfizer. G.G-M. declares research support from and an advisory role at Bristol Myers Squibb, Astex, and Helsinn, and research support from Amphivena, Novartis, AbbVie, H3 Biomedicine, Onconova, and Merck. S.C. declares research support from Amgen.

DECLARATION OF GENERATIVE AI AND AI-ASSISTED TECHNOLOGIES IN THE WRITING PROCESS

During the preparation of this work, S.C. used Grammarly to correct grammar mistakes. After using this tool, S.C. reviewed and edited the content as needed. S.C. takes full responsibility for the content of the publication.

Received: December 4, 2022
Revised: November 27, 2023
Accepted: April 30, 2024
Published: May 22, 2024

REFERENCES

1. Itzykson, R., Kosmider, O., Renneville, A., Morabito, M., Preudhomme, C., Berthon, C., Adès, L., Fenaux, P., Platzbecker, U., Gagey, O., et al. (2013). Clonal architecture of chronic myelomonocytic leukemias. Blood *121*, 2186–2198. https://doi.org/10.1182/blood-2012-06-440347.
2. Arber, D.A., Orazi, A., Hasserjian, R., Thiele, J., Borowitz, M.J., Le Beau, M.M., Bloomfield, C.D., Cazzola, M., and Vardiman, J.W. (2016). The 2016 revision to the World Health Organization classification of myeloid neoplasms and acute leukemia. Blood *127*, 2391–2405. https://doi.org/10.1182/blood-2016-03-643544.
3. Vardiman, J.W., Thiele, J., Arber, D.A., Brunning, R.D., Borowitz, M.J., Porwit, A., Harris, N.L., Le Beau, M.M., Hellström-Lindberg, E., Tefferi, A., and Bloomfield, C.D. (2009). The 2008 revision of the World Health Organization (WHO) classification of myeloid neoplasms and acute leukemia: rationale and important changes. Blood *114*, 937–951. https://doi.org/10.1182/blood-2009-03-209262.
4. Patnaik, M.M., Padron, E., LaBorde, R.R., Lasho, T.L., Finke, C.M., Hanson, C.A., Hodnefield, J.M., Knudson, R.A., Ketterling, R.P., Al-kali, A., et al. (2013). Mayo prognostic model for whom-defined chronic myelomonocytic leukemia: ASXL1 and spliceosome component mutations and outcomes. Leukemia *27*, 1504–1510. https://doi.org/10.1038/leu.2013.88.
5. Onida, F., Kantarjian, H.M., Smith, T.L., Ball, G., Keating, M.J., Estey, E.H., Glassman, A.B., Albitar, M., Kwari, M.I., and Beran, M. (2002). Prognostic factors and scoring systems in chronic myelomonocytic leukemia: a retrospective analysis of 213 patients. Blood *99*, 840–849.
6. Patnaik, M.M., Itzykson, R., Lasho, T.L., Kosmider, O., Finke, C.M., Hanson, C.A., Knudson, R.A., Ketterling, R.P., Tefferi, A., and Solary, E. (2014). ASXL1 and SETBP1 mutations and their prognostic contribution in chronic myelomonocytic leukemia: a two-center study of 466 patients. Leukemia *28*, 2206–2212. https://doi.org/10.1038/leu.2014.125.
7. Pleyer, L., Leisch, M., Kourakli, A., Padron, E., Maciejewski, J.P., Xicoy Cirici, B., Kaivers, J., Ungerstedt, J., Heibl, S., Patiou, P., et al. (2021). Outcomes of patients with chronic myelomonocytic leukaemia treated with non-curative therapies: a retrospective cohort study. Lancet. Haematol. *8*, e135–e148. https://doi.org/10.1016/S2352-3026(20)30374-4.
8. Alfonso, A., Montalban-Bravo, G., Takahashi, K., Jabbour, E.J., Kadia, T., Ravandi, F., Cortes, J., Estrov, Z., Borthakur, G., Pemmaraju, N., et al. (2017). Natural history of chronic myelomonocytic leukemia treated with hypomethylating agents. Am. J. Hematol. *92*, 599–606. https://doi.org/10.1002/ajh.24735.
9. Montalban-Bravo, G., Kanagal-Shamanna, R., Li, Z., Hammond, D., Chien, K., Rodriguez-Sevilla, J.J., Sasaki, K., Jabbour, E., DiNardo, C., Takahashi, K., et al. (2023). Phenotypic subtypes of leukaemic transformation in chronic myelomonocytic leukaemia. Br. J. Haematol. *203*, 581–592. https://doi.org/10.1111/bjh.19060.
10. Itzykson, R., Kosmider, O., Renneville, A., Gelsi-Boyer, V., Meggendorfer, M., Morabito, M., Berthon, C., Adès, L., Fenaux, P., Beyne-Rauzy, O., et al. (2013). Prognostic score including gene mutations in chronic myelomonocytic leukemia. J. Clin. Oncol. *31*, 2428–2436. https://doi.org/10.1200/JCO.2012.47.3314.
11. Montalban-Bravo, G., Hammond, D., DiNardo, C.D., Konopleva, M., Borthakur, G., Short, N.J., Ramos-Perez, J., Guerra, V., Kanagal-Shamanna, R., Naqvi, K., et al. (2021). Activity of venetoclax-based therapy in chronic myelomonocytic leukemia. Leukemia *35*, 1494–1499. https://doi.org/10.1038/s41375-021-01240-2.
12. Paul, F., Arkin, Y., Giladi, A., Jaitin, D.A., Kenigsberg, E., Keren-Shaul, H., Winter, D., Lara-Astiaso, D., Gury, M., Weiner, A., et al. (2015). Transcriptional Heterogeneity and Lineage Commitment in Myeloid Progenitors. Cell *163*, 1663–1677. https://doi.org/10.1016/j.cell.2015.11.013.
13. Giladi, A., Paul, F., Herzog, Y., Lubling, Y., Weiner, A., Yofe, I., Jaitin, D., Cabezas-Wallscheid, N., Dress, R., Ginhoux, F., et al. (2018). Single-cell characterization of haematopoietic progenitors and their trajectories in homeostasis and perturbed haematopoiesis. Nat. Cell Biol. *20*, 836–846. https://doi.org/10.1038/s41556-018-0121-4.
14. Lian, Q., Xin, H., Ma, J., Konnikova, L., Chen, W., Gu, J., and Chen, K. (2020). Artificial-cell-type aware cell-type classification in CITE-seq. Bioinformatics *36*, i542–i550. https://doi.org/10.1093/bioinformatics/btaa467.
15. Zhou, Z., Ye, C., Wang, J., and Zhang, N.R. (2020). Surface protein imputation from single cell transcriptomes by deep neural networks. Nat. Commun. *11*, 651. https://doi.org/10.1038/s41467-020-14391-0.
16. Hamarsheh, S., Groß, O., Brummer, T., and Zeiser, R. (2020). Immune modulatory effects of oncogenic KRAS in cancer. Nat. Commun. *11*, 5439. https://doi.org/10.1038/s41467-020-19288-6.
17. Efremova, M., Vento-Tormo, M., Teichmann, S.A., and Vento-Tormo, R. (2020). CellPhoneDB: inferring cell-cell communication from combined expression of multi-subunit ligand-receptor complexes. Nat. Protoc. *15*, 1484–1506. https://doi.org/10.1038/s41596-020-0292-x.

18. Chenette, E.J. (2009). Cancer: A Ras and NF-kappaB pas de deux. Nat. Rev. Drug Discov. *8*, 932. https://doi.org/10.1038/nrd3060.

19. Datta, J., Bianchi, A., De Castro Silva, I., Deshpande, N.U., Cao, L.L., Mehra, S., Singh, S., Rafie, C., Sun, X., Chen, X., et al. (2022). Distinct mechanisms of innate and adaptive immune regulation underlie poor oncologic outcomes associated with KRAS-TP53 co-alteration in pancreatic cancer. Oncogene *41*, 3640–3654. https://doi.org/10.1038/s41388-022-02368-w.

20. Daniluk, J., Liu, Y., Deng, D., Chu, J., Huang, H., Gaiser, S., Cruz-Monserrate, Z., Wang, H., Ji, B., and Logsdon, C.D. (2012). An NF-kappaB pathway-mediated positive feedback loop amplifies Ras activity to pathological levels in mice. J. Clin. Invest. *122*, 1519–1528. https://doi.org/10.1172/JCI59743.

21. Hamarsheh, S., Osswald, L., Saller, B.S., Unger, S., De Feo, D., Vinnakota, J.M., Konantz, M., Uhl, F.M., Becker, H., Lübbert, M., et al. (2020). Oncogenic Kras(G12D) causes myeloproliferation via NLRP3 inflammasome activation. Nat. Commun. *11*, 1659. https://doi.org/10.1038/s41467-020-15497-1.

22. Morandi, F., Airoldi, I., and Pistoia, V. (2014). IL-27 driven upregulation of surface HLA-E expression on monocytes inhibits IFN-gamma release by autologous NK cells. J. Immunol. Res. *2014*, 938561. https://doi.org/10.1155/2014/938561.

23. Pereira, B.I., Devine, O.P., Vukmanovic-Stejic, M., Chambers, E.S., Subramanian, P., Patel, N., Virasami, A., Sebire, N.J., Kinsler, V., Valdovinos, A., et al. (2019). Senescent cells evade immune clearance via HLA-E-mediated NK and CD8(+) T cell inhibition. Nat. Commun. *10*, 2387. https://doi.org/10.1038/s41467-019-10335-5.

24. Ramsuran, V., Naranbhai, V., Horowitz, A., Qi, Y., Martin, M.P., Yuki, Y., Gao, X., Walker-Sperling, V., Del Prete, G.Q., Schneider, D.K., et al. (2018). Elevated HLA-A expression impairs HIV control through inhibition of NKG2A-expressing cells. Science *359*, 86–90. https://doi.org/10.1126/science.aam8825.

25. Banh, C., Fugère, C., and Brossay, L. (2009). Immunoregulatory functions of KLRG1 cadherin interactions are dependent on forward and reverse signaling. Blood *114*, 5299–5306. https://doi.org/10.1182/blood-2009-06-228353.

26. Lou, C., Wu, K., Shi, J., Dai, Z., and Xu, Q. (2022). N-cadherin protects oral cancer cells from NK cell killing in the circulation by inducing NK cell functional exhaustion via the KLRG1 receptor. J. Immunother. Cancer *10*, e005061. https://doi.org/10.1136/jitc-2022-005061.

27. Yang, R., Sun, L., Li, C.F., Wang, Y.H., Yao, J., Li, H., Yan, M., Chang, W.C., Hsu, J.M., Cha, J.H., et al. (2021). Galectin-9 interacts with PD-1 and TIM-3 to regulate T cell death and is a target for cancer immunotherapy. Nat. Commun. *12*, 832. https://doi.org/10.1038/s41467-021-21099-2.

28. Slattery, K., Woods, E., Zaiatz-Bittencourt, V., Marks, S., Chew, S., Conroy, M., Goggin, C., MacEochagain, C., Kennedy, J., Lucas, S., et al. (2021). TGFbeta drives NK cell metabolic dysfunction in human metastatic breast cancer. J. Immunother. Cancer *9*, e002044. https://doi.org/10.1136/jitc-2020-002044.

29. Chakravarthy, A., Khan, L., Bensler, N.P., Bose, P., and De Carvalho, D.D. (2018). TGF-beta-associated extracellular matrix genes link cancer-associated fibroblasts to immune evasion and immunotherapy failure. Nat. Commun. *9*, 4692. https://doi.org/10.1038/s41467-018-06654-8.

30. Yu, L., Liu, X., Wang, X., Yan, F., Wang, P., Jiang, Y., Du, J., and Yang, Z. (2021). TIGIT(+) TIM-3(+) NK cells are correlated with NK cell exhaustion and disease progression in patients with hepatitis B virusrelated hepatocellular carcinoma. OncoImmunology *10*, 1942673. https://doi.org/10.1080/2162402X.2021.1942673.

31. Juno, J.A., Stalker, A.T., Waruk, J.L., Oyugi, J., Kimani, M., Plummer, F.A., Kimani, J., and Fowke, K.R. (2015). Elevated expression of LAG-3, but not PD-1, is associated with impaired iNKT cytokine production during chronic HIV-1 infection and treatment. Retrovirology *12*, 17. https://doi.org/10.1186/s12977-015-0142-z.

32. Chan, I.S., Knutsdottir, H., Ramakrishnan, G., Padmanaban, V., Warrier, M., Ramirez, J.C., Dunworth, M., Zhang, H., Jaffee, E.M., Bader, J.S., and Ewald, A.J. (2020). Cancer cells educate natural killer cells to a metastasis-promoting cell state. J. Cell Biol. *219*. https://doi.org/10.1083/jcb.202001134.

33. Corces, M.R., Buenrostro, J.D., Wu, B., Greenside, P.G., Chan, S.M., Koenig, J.L., Snyder, M.P., Pritchard, J.K., Kundaje, A., Greenleaf, W.J., et al. (2016). Lineage-specific and single-cell chromatin accessibility charts human hematopoiesis and leukemia evolution. Nat. Genet. *48*, 1193–1203. https://doi.org/10.1038/ng.3646.

34. Caenepeel, S., Brown, S.P., Belmontes, B., Moody, G., Keegan, K.S., Chui, D., Whittington, D.A., Huang, X., Poppe, L., Cheng, A.C., et al. (2018). AMG 176, a Selective MCL1 Inhibitor, Is Effective in Hematologic Cancer Models Alone and in Combination with Established Therapies. Cancer Discov. *8*, 1582–1597. https://doi.org/10.1158/2159-8290.CD-18-0387.

35. Awada, H., Nagata, Y., Goyal, A., Asad, M.F., Patel, B., Hirsch, C.M., Kuzmanovic, T., Guan, Y., Przychodzen, B.P., Aly, M., et al. (2019). Invariant phenotype and molecular association of biallelic TET2 mutant myeloid neoplasia. Blood Adv. *3*, 339–349. https://doi.org/10.1182/bloodadvances.2018024216.

36. Carr, R.M., Vorobyev, D., Lasho, T., Marks, D.L., Tolosa, E.J., Vedder, A., Almada, L.L., Yurcheko, A., Padioleau, I., Alver, B., et al. (2021). RAS mutations drive proliferative chronic myelomonocytic leukemia via a KMT2A-PLK1 axis. Nat. Commun. *12*, 2901. https://doi.org/10.1038/s41467-021-23186-w.

37. Zhang, Y., He, L., Selimoglu-Buet, D., Jego, C., Morabito, M., Willekens, C., Diop, M.K., Gonin, P., Lapierre, V., Droin, N., et al. (2017). Engraftment of chronic myelomonocytic leukemia cells in immunocompromised mice supports disease dependency on cytokines. Blood Adv. *1*, 972–979. https://doi.org/10.1182/bloodadvances.2017004903.

38. Patel, B.J., Przychodzen, B., Thota, S., Radivoyevitch, T., Visconte, V., Kuzmanovic, T., Clemente, M., Hirsch, C., Morawski, A., Souaid, R., et al. (2017). Genomic determinants of chronic myelomonocytic leukemia. Leukemia *31*, 2815–2823. https://doi.org/10.1038/leu.2017.164.

39. Montalban-Bravo, G., Hammond, D., DiNardo, C.D., Konopleva, M., Borthakur, G., Short, N.J., Ramos-Perez, J., Guerra, V., Kanagal-Shamanna, R., Naqvi, K., et al. (2021). Activity of venetoclax-based therapy in chronic myelomonocytic leukemia. Leukemia *35*, 1494–1499. https://doi.org/10.1038/s41375-021-01240-2.

40. Reggiardo, R.E., Maroli, S.V., Halasz, H., Ozen, M., Hrabeta-Robinson, E., Behera, A., Peddu, V., Carrillo, D., LaMontagne, E., Whitehead, L., et al. (2022). Mutant KRAS regulates transposable element RNA and innate immunity via KRAB zinc-finger genes. Cell Rep. *40*, 111104. https://doi.org/10.1016/j.celrep.2022.111104.

41. Ferrall-Fairbanks, M.C., Dhawan, A., Johnson, B., Newman, H., Volpe, V., Letson, C., Ball, M., Hunter, A.M., Balasis, M.E., Kruer, T., et al. (2022). Progenitor Hierarchy of Chronic Myelomonocytic Leukemia Identifies Inflammatory Monocytic-Biased Trajectory Linked to Worse Outcomes. Blood Cancer Discov. *3*, 536–553. https://doi.org/10.1158/2643-3230.BCD-21-0217.

42. Chen, X., Eksioglu, E.A., Zhou, J., Zhang, L., Djeu, J., Fortenbery, N., Epling-Burnette, P., Van Bijnen, S., Dolstra, H., Cannon, J., et al. (2013). Induction of myelodysplasia by myeloid-derived suppressor cells. J. Clin. Invest. *123*, 4595–4611. https://doi.org/10.1172/JCI67580.

43. Garcia-Manero, G., Winer, E.S., DeAngelo, D.J., Tarantolo, S.R., Sallman, D.A., Dugan, J., Groepper, S., Giagounidis, A., Gotze, K.S., Metzeler, K., et al. (2022). Phase 1/2a study of the IRAK4 inhibitor CA-4948 as monotherapy or in combination with azacitidine or venetoclax in patients with relapsed/refractory (R/R) acute myeloid leukemia or lyelodysplastic syndrome. J. Clin. Oncol. *40*, 7016. https://doi.org/10.1200/JCO.2022.40.16_suppl.7016.

44. Hunter, A.M., Newman, H., Dezern, A.E., Steensma, D.P., Niyongere, S., Roboz, G.J., Mo, Q., Chan, O., Gerds, A., Sallman, D.A., et al. (2021).

Integrated Human and Murine Clinical Study Establishes Clinical Efficacy of Ruxolitinib in Chronic Myelomonocytic Leukemia. Clin. Cancer Res. *27*, 6095–6105. https://doi.org/10.1158/1078-0432.CCR-21-0935.

45. Walker, A.R., Byrd, J.C., Blachly, J.S., Bhatnagar, B., Mims, A.S., Orwick, S., Lin, T.L., Crosswell, H.E., Zhang, D., Minden, M.D., et al. (2020). Entospletinib in Combination with Induction Chemotherapy in Previously Untreated Acute Myeloid Leukemia: Response and Predictive Significance of HOXA9 and MEIS1 Expression. Clin. Cancer Res. *26*, 5852–5859. https://doi.org/10.1158/1078-0432.CCR-20-1064.

46. Ganan-Gomez, I., Yang, H., Ma, F., Montalban-Bravo, G., Thongon, N., Marchica, V., Richard-Carpentier, G., Chien, K., Manyam, G., Wang, F., et al. (2022). Stem cell architecture drives myelodysplastic syndrome progression and predicts response to venetoclax-based therapy. Nat. Med. *28*, 557–567. https://doi.org/10.1038/s41591-022-01696-4.

47. Tago, K., Funakoshi-Tago, M., Ohta, S., Kawata, H., Saitoh, H., Horie, H., Aoki-Ohmura, C., Yamauchi, J., Tanaka, A., Matsugi, J., and Yanagisawa, K. (2019). Oncogenic Ras mutant causes the hyperactivation of NF-kappaB via acceleration of its transcriptional activation. Mol. Oncol. *13*, 2493–2510. https://doi.org/10.1002/1878-0261.12580.

48. Sevin, M., Debeurme, F., Laplane, L., Badel, S., Morabito, M., Newman, H.L., Torres-Martin, M., Yang, Q., Badaoui, B., Wagner-Ballon, O., et al. (2021). Cytokine-like protein 1-induced survival of monocytes suggests a combined strategy targeting MCL1 and MAPK in CMML. Blood *137*, 3390–3402. https://doi.org/10.1182/blood.2020008729.

49. Pei, S., Pollyea, D.A., Gustafson, A., Stevens, B.M., Minhajuddin, M., Fu, R., Riemondy, K.A., Gillen, A.E., Sheridan, R.M., Kim, J., et al. (2020). Monocytic Subclones Confer Resistance to Venetoclax-Based Therapy in Patients with Acute Myeloid Leukemia. Cancer Discov. *10*, 536–551. https://doi.org/10.1158/2159-8290.CD-19-0710.

50. Hao, Y., Hao, S., Andersen-Nissen, E., Mauck, W.M., 3rd, Zheng, S., Butler, A., Lee, M.J., Wilk, A.J., Darby, C., Zager, M., et al. (2021). Integrated analysis of multimodal single-cell data. Cell *184*, 3573–3587.e29. https://doi.org/10.1016/j.cell.2021.04.048.

51. Vento-Tormo, R., Efremova, M., Botting, R.A., Turco, M.Y., Vento-Tormo, M., Meyer, K.B., Park, J.-E., Stephenson, E., Polański, K., Goncalves, A., et al. (2018). Single-cell reconstruction of the early maternal–fetal interface in humans. Nature *563*, 347–353. https://doi.org/10.1038/s41586-018-0698-6.

52. Kanagal-Shamanna, R., Singh, R.R., Routbort, M.J., Patel, K.P., Medeiros, L.J., and Luthra, R. (2016). Principles of analytical validation of next-generation sequencing based mutational analysis for hematologic neoplasms in a CLIA-certified laboratory. Expert Rev. Mol. Diagn. *16*, 461–472. https://doi.org/10.1586/14737159.2016.1142374.

53. DeLong, E.R., DeLong, D.M., and Clarke-Pearson, D.L. (1988). Comparing the areas under two or more correlated receiver operating characteristic curves: a nonparametric approach. Biometrics *44*, 837–845.

54. Cheson, B.D., Bennett, J.M., Kopecky, K.J., Büchner, T., Willman, C.L., Estey, E.H., Schiffer, C.A., Doehner, H., Tallman, M.S., Lister, T.A., et al. (2003). Revised recommendations of the International Working Group for Diagnosis, Standardization of Response Criteria, Treatment Outcomes, and Reporting Standards for Therapeutic Trials in Acute Myeloid Leukemia. J. Clin. Oncol. *21*, 4642–4649. https://doi.org/10.1200/JCO.2003.04.036.

55. Cheson, B.D., Greenberg, P.L., Bennett, J.M., Lowenberg, B., Wijermans, P.W., Nimer, S.D., Pinto, A., Beran, M., de Witte, T.M., Stone, R.M., et al. (2006). Clinical application and proposal for modification of the International Working Group (IWG) response criteria in myelodysplasia. Blood *108*, 419–425. https://doi.org/10.1182/blood-2005-10-4149.

56. Woll, P.S., Kjällquist, U., Chowdhury, O., Doolittle, H., Wedge, D.C., Thongjuea, S., Erlandsson, R., Ngara, M., Anderson, K., Deng, Q., et al. (2014). Myelodysplastic syndromes are propagated by rare and distinct human cancer stem cells in vivo. Cancer Cell *25*, 794–808. https://doi.org/10.1016/j.ccr.2014.03.036.

57. Will, B., Zhou, L., Vogler, T.O., Ben-Neriah, S., Schinke, C., Tamari, R., Yu, Y., Bhagat, T.D., Bhattacharyya, S., Barreyro, L., et al. (2012). Stem and progenitor cells in myelodysplastic syndromes show aberrant stage-specific expansion and harbor genetic and epigenetic alterations. Blood *120*, 2076–2086. https://doi.org/10.1182/blood-2011-12-399683.

58. Adema, V., Ma, F., Kanagal-Shamanna, R., Thongon, N., Montalban-Bravo, G., Yang, H., Peslak, S.A., Wang, F., Acha, P., Sole, F., et al. (2022). Targeting the EIF2AK1 signaling pathway rescues red blood cell production in SF3B1-mutant myelodysplastic syndromes with ringed sideroblasts. Blood Cancer Discov. *3*, 554–567. https://doi.org/10.1158/2643-3230.BCD-21-0220.

59. Zhou, Y., Zhou, B., Pache, L., Chang, M., Khodabakhshi, A.H., Tanaseichuk, O., Benner, C., and Chanda, S.K. (2019). Metascape provides a biologist-oriented resource for the analysis of systems-level datasets. Nat. Commun. *10*, 1523. https://doi.org/10.1038/s41467-019-09234-6.

60. Thongon, N., Ma, F., Santoni, A., Marchesini, M., Fiorini, E., Rose, A., Adema, V., Ganan-Gomez, I., Groarke, E.M., Gutierrez-Rodrigues, F., et al. (2021). Hematopoiesis under telomere attrition at the single-cell resolution. Nat. Commun. *12*, 6850. https://doi.org/10.1038/s41467-021-27206-7.

61. Buenrostro, J.D., Corces, M.R., Lareau, C.A., Wu, B., Schep, A.N., Aryee, M.J., Majeti, R., Chang, H.Y., and Greenleaf, W.J. (2018). Integrated Single-Cell Analysis Maps the Continuous Regulatory Landscape of Human Hematopoietic Differentiation. Cell *173*, 1535–1548.e16. https://doi.org/10.1016/j.cell.2018.03.074.

62. Morita, K., Wang, F., Jahn, K., Hu, T., Tanaka, T., Sasaki, Y., Kuipers, J., Loghavi, S., Wang, S.A., Yan, Y., et al. (2020). Clonal evolution of acute myeloid leukemia revealed by high-throughput single-cell genomics. Nat. Commun. *11*, 5327. https://doi.org/10.1038/s41467-020-19119-8.

STAR★METHODS

KEY RESOURCES TABLE

REAGENT or RESOURCE	SOURCE	IDENTIFIER
Antibodies		
Anti-human CD2	BD Biosciences	Cat#: 555326; RRID: AB_395733
Anti-human CD3	BD Biosciences	Cat#: 349201; RRID: AB_400405
Anti-human CD4	ThermoFisher	Cat#: MHCD0401; RRID:AB_10392546
Anti-human CD7	BioLegend	Cat#: 343104; RRID: AB_1659216
Anti-human CD11b	ThermoFisher	Cat#: 11-0118-42; RRID: AB_1582242
anti-human CD14	BD Biosciences	Cat#: 347493; RRID: AB_400311
Anti-human CD19	BD Biosciences	Cat#: 340409; RRID: AB_400024
Anti-human CD20	BD Biosciences	Cat#: 555622; RRID: AB_395988
Anti-human CD33	ThermoFisher	Cat#: 11-0337-42; RRID: AB_1603221
Anti-human CD56	BD Biosciences	Cat#: 562794; RRID: AB_2737799
Anti-human CD235	BD Biosciences	Cat#: 559943; RRID: AB_397386
Anti-human CD34	BD Biosciences	Cat#: 562577; RRID: AB_2687922
Anti-human CD38	BioLegend	Cat#: 303534; RRID: AB_2561605
Anti-human CD3	BioLegend	Cat#: 317339; RRID: AB_2563407
Anti-human CD4	BioLegend	Cat#: 300502; RRID: AB_314070
Anti-human CD8	BioLegend	Cat#: 344710; RRID: AB_2044010
Anti-human CD56	BioLegend	Cat#: 362544; RRID: AB_2565922
Anti-human CD16	BioLegend	Cat#: 302028; RRID: AB_893262
Anti-Human IFN-γ	BD Biosciences	Cat#: 554702; RRID: AB_398580
Anti-human Perforin	BioLegend	Cat#: 308130; RRID: AB_2687190
Zombie UV	BioLegend	Cat#: 423107
Protein Transport Inhibitor Cocktail	eBioscience	Cat#: 00-4980-93
Fc Receptor Binding Inhibitor Polyclonal Antibody	ThermoFisher	Cat#: 14-9161-73
CD3e	Cell Signaling Technology	Cat#: 85061BF; RRID: AB_2721019
CD4	Abcam	Cat#: ab133616; RRID: AB_2750883
CD8	Thermo Scientific	Catalog#: MA5-13473; RRID: AB_11000353
CD14	Abcam	Cat#: ab183322; RRID: AB_2909463
CD68, Clone PG-M1	Dako	Cat#: M0876; RRID: AB_2074844
CD56	Dako	Cat#: M7304; RRID: AB_2750583
DAPI	Akoya Biosciences	Cat#: FP1490; RRID: N/A
MCL1	Cell Signaling Technology	Cat#: 4572; RRID:AB_2281980
Vinculin	Sigma-Aldrich	Cat#: V9131; RRID:AB_477629
Biological samples		
Bone marrow aspirates from healthy donors	AllCells (Alameda, CA) and MD Anderson's Department of Stem Cell Transplantation	N/A
Bone marrow aspirates from CMML patients	MD Anderson Bank	N/A
Human bone marrow-derived mesenchymal stem cells	Cells provided by Dr. M. Andreeff	N/A
Chemicals, peptides, and recombinant proteins		
AMG-176	Med Chem Express	Cat#: HY-101565

(Continued on next page)

Continued

REAGENT or RESOURCE	SOURCE	IDENTIFIER
Critical commercial assays		
Cytofix/Cytoperm kit	BD Biosciences	Cat#: 554714
Deposited data		
scRNA-seq data	This paper	GEO: GSE218390
scATAC-seq data	This paper	GEO: GSE218390
scDNA-seq data	This paper	GEO: GSE218390
Experimental models: Cell lines		
K562 cells	ATCC	ATCC CCL243
Software and algorithms		
SPSS 23.0	SPSS, Inc	https://www.ibm.com/products/spss-statistics
R v4.1.2	R Core Team	https://www.r-project.org
Seurat v4 R package ‘	Hao et al.[50]	https://github.com/satijalab/seurat
CellphoneDB	Vento-Tormo et al.[51]	https://www.cellphonedb.org/
GraphPad Prism version 10.0	GraphPad software	https://www.graphpad.com/
Spotfire	TIBCO	N/A
FlowJo	BD Biosciences	https://www.flowjo.com/
GSEA	Metascape	https://metascape.org/
Spotfire	TIBCO	https://www.spotfire.com/
Other		
Ficoll-Paque PLUS	ThermoFisher	Cat#:45-001-752
CD34 Microbead Kit	Miltenyi Biotec	Cat#:130-046-702
NK Cell Isolation Kit	Miltenyi Biotec	Cat#: 130-092-657
Opal 9 Kit	Akoya Biosciences	Cat#: NEL797001KT
Qubit	Thermo Fisher Scientific	N/A

RESOURCE AVAILABILITY

Lead contact

Further information and requests for resources and reagents should be directed to and will be fulfilled by the lead contact, Simona Colla (scolla@mdanderson.org).

Materials availability

This study did not generate new unique reagents.

Data and code availability

- scRNA-seq, scATAC-seq, and scDNA-seq data are accessible at GEO under accession number GSE218390. No custom computer codes were generated in this study.
- The lead contact can provide any additional information required to reanalyze the data reported in this work paper upon request.

EXPERIMENTAL MODEL AND STUDY PARTICIPANT DETAILS

Primary human samples

BM aspirates were obtained from patients with CMML who were seen in the Department of Leukemia at the University of Texas MD Anderson Cancer Center. Samples were obtained with the approval of the Institutional Review Board and in accordance with the Declaration of Helsinki. CMML diagnoses were assigned according to the World Health Organization criteria.[3]

RAS pathway mutations were identified by targeted amplicon-based next-generation sequencing (NSG).[52] Genomic DNA was extracted from whole BM aspirate samples and was subject to targeted PCR-based sequencing using an NGS platform evaluating a total of 81 genes, as previously described.[52] This analysis was performed within the MDACC CLIA-certified Molecular Diagnostics Laboratory after informed consent (additional details in supplemental information). For NGS-based analysis, the limit of detection for variant calling was 2%. Previously described somatic mutations registered at the Catalog of Somatic Mutations in Cancer (COSMIC: http://cancer.sanger.ac.uk/cosmic) were considered potential driver mutations.

All available samples carrying *RAS* pathway mutations were included in the study. Baseline BM aspirates were collected from patients before any treatment. Sequential BM samples were collected after HMA or venetoclax therapy failure. The clinical characteristics of the patients with *RAS* pathway mutated CMML are shown in Tables S1 and S3. BM samples from HDs were obtained from AllCells (Alameda, CA) and the Department of Stem Cell Transplantation at MD Anderson Cancer Center. Written informed consent was obtained from all donors.

MNCs were collected from each BM sample immediately after BM aspiration using the standard gradient separation approach with Ficoll-Paque PLUS (catalog number #45-001-752, Thermo Fisher Scientific). MNCs were cryopreserved and stored in liquid nitrogen until they were used. For cell sorting applications, MNCs were enriched in CD34$^+$ cells using magnetic-activated cell sorting (MACS) with the CD34 Microbead Kit (catalog number #130-046-702, Miltenyi Biotec, Germany) and further purified by fluorescence-activated cell sorting (FACS) as described below.

METHOD DETAILS

Clinical data analysis

A clinical dataset of 108 CMML patients treated with HMA therapy at the Department of Leukemia at the University of Texas MD Anderson Cancer Center was evaluated to identify predictors of therapy outcomes. HMA therapy failure was defined as a lack of response (based on IWG 2006 criteria) after at least 4 cycles of therapy or as relapse or progression after any number of cycles of therapy. Blast progression (BP) was defined as 1) the presence of >5% blasts in the BM at the time of primary HMA failure in patients with <5% blasts at baseline or an increase of at least 50% blasts in patients with 5–9% blasts at baseline; 2) BM blasts >20% or myeloid sarcoma regardless of primary or secondary failure; 3) BM blasts >5% at the time of secondary HMA failure (relapse or progression). Associations between gene mutations and BP were assessed using data from 108 patients whose samples were sequenced using the 81-gene panel; these analyses were performed at MD Anderson Cancer Center. Clinical datasets were analyzed using the SPSS 23.0 (SPSS, Inc., Chicago, IL, USA) and R (version 3.5.1) statistical software programs. Logistical regression analysis was performed using clinical, cytogenetic, and molecular characteristics in correlation with responses to HMA therapy. The dataset was randomly divided into a training set (30 patients with BP) and a testing set (5 patients with BP). A combination rule derived from selected features was trained using logistic regression in the training set and a fixed model in the testing set. Receiver operating characteristic (ROC) curves were generated using the “pROC” package in R (version 3.6.0). The 95% CIs for the areas under the ROC curves were estimated using the DeLong method.[53] The chi-square or Fisher exact test was used to analyze differences between categorical variables. Survival curves were generated using the Kaplan-Meier method and compared using log rank tests. Responses to HMA- or venetoclax-based therapies were evaluated based on the International Working group 2003[54] and 2006[55] criteria for patients with secondary AML or CMML, respectively.

Flow cytometry analysis and fluorescence-activated cell sorting (FACS)

Quantitative flow cytometry and FACS analyses of Lin$^-$CD34$^+$ cells were performed using previously described staining protocols[56,57] and antibodies against CD2, FITC, RPA-2.10, BD Biosciences, 555326; CD3, FITC, SK7, BD Biosciences, 349201; CD4, FITC, S3.5, Thermo Fisher, MHCD0401; CD7, FITC, 6B7, BioLegend, 343104; CD11b, FITC, ICRF44, Thermo Fisher, 11-0118-42; CD14, FITC, MφP9, BD Biosciences, 347493; CD19, FITC, SJ25C1, BD Biosciences, 340409; CD20, FITC, 2H7, BD Biosciences, 555622; CD33, FITC, P67.6, Thermo Fisher, 11-0337-42; CD56, FITC, B159, BD Biosciences, 562794; CD235a, FITC, HIR2, BD Biosciences, 559943; CD34, BV421, 581, BD Biosciences, 562577; CD38, APC, HIT2, BioLegend, 303534, as we described previously.[58]

Samples used for flow cytometry and FACS were acquired with a BD LSR Fortessa and a BD Influx Cell Sorter (BD Biosciences), respectively. The cell populations were analyzed using FlowJo software (https://www.flowjo.com). All experiments included single-stained controls and were performed at the South Campus Flow Cytometry & Cellular Imaging Facility at MD Anderson Cancer Center.

Multiplex imaging assay

BM core biopsies were used for multiplex immunofluorescence assessment. We optimized and validated a multiplex immunofluorescence panel using antibodies against CD3e, CD4, CD8, CD14, CD56, and CD68. Each antibody was assessed by multiplex immunofluorescence using the Opal 9 kit (catalog #NEL797001KT; Akoya Biosciences, Marlborough, MA), according to the following clones and dilutions: CD3e (clone D7A6E(AM), Cell Signaling Technology, 1:100), CD4 (clone EPR6855, Abcam, 1:200), CD8 (clone C8/144B, Thermo Scientific, 1:25), CD14 (clone SP192, Abcam, 1:100), CD56 (clone 123C3, Dako, 1:25), and CD68 (clone PG-M1, Dako, 1:50). The slides were imaged using the Vectra Polaris spectral imaging system (Akoya Biosciences, Marlborough, MA) using the fluorescence protocol at 10 nm λ from 420 nm to 720 nm. Both germinal center and interfollicular areas from lymph nodes with reactive lymphoid hyperplasia were used as positive controls. Each marker was analyzed at the single-cell level, and a supervised algorithm for phenotyping was built for each marker. Cell density for each marker and combinations of phenotypes were consolidated using Spotfire software (TIBCO Spotfire). The nearest neighbor analysis was performed using R version 4.2.1.

Western blot

BM $CD34^+$ cells were enriched from BM MNCs using magnetic sorting with the CD34 Microbead Kit (Miltenyi Biotec). Cells were resuspended in Mammalian Cell & Tissue Extraction Kit buffer (BioVision Incorporated) and incubated on ice for 10 min. Lysates were then collected after centrifugation at 12,000 rpm at 4°C for 20 min. The amount of protein was quantified using the Qubit Protein Assay Kit and a Qubit Fluorometer (Thermo Fisher Scientific). SDS-PAGE and Western blotting were performed following standard protocols. Blotted membranes were incubated with primary monoclonal antibodies against human MCL1 (#4572S; 1:750 dilution; Cell Signaling Technology) and vinculin (hVIN-1; 1:2,000 dilution; Sigma-Aldrich). Membranes were developed using the SuperSignal West Pico PLUS Chemiluminescent Substrate (Thermo Fisher Scientific) in a KwikQuant Imager (Kindle Biosciences). Vinculin was used as a loading control, and lysates from the myeloma cell line JJN3 were used as positive controls.

T cell and NK cell cytokine secretion assays

NK cells were isolated from BM MNCs obtained from HDs, and *RAS* pathway mutant or wild-type CMML patients by negative magnetic selection using the NK Cell Isolation Kit (Miltenyi Biotec). NK cells or BM MNCs were mixed with the human erythroleukemia cell line K562 at a target-to-effector ratio of 1:1. Cells were incubated for 4h at 37°C in 5% CO_2 in the presence of a protein transport inhibitor cocktail (eBioscience 00-4980-93) for 4 h. After incubation, cells were harvested, washed with PBS, and stained with the viability dye Zombie UV. Cells were washed with PBS and resuspended in the presence of an Fc receptor-binding inhibitor antibody (ThermoFisher) for 20 min. NK cells and BM MNCs were stained with antibodies against CD3 (AF700, BioLegend). NK cells were further stained with antibodies against CD56 (PE-Dazle 594) and CD16 (PerCP-Cy5.5), whereas BM MNCs were stained with antibodies against CD4 (PE-Dazzle 594) and CD8 (PerCP-Cy5.5). Cells were then washed, fixed, and permeabilized using the Cytofix/Cytoperm kit (BD Biosciences) and intracellularly stained with antibodies against IFN-γ (APC, BD Biosciences) and perforin (BV711, BioLegend). Samples were acquired with a BD Fortessa (BD Biosciences), and cell populations were analyzed using FlowJo software (version 10.7.1, Ashland, OR).

scRNA-seq analysis and bioinformatic pipeline

ScRNA-seq analysis was performed as we described previously.[58] Live Lin^-CD34^+ cells and live MNCs were isolated by FACS. Sample preparation and sequencing were performed at the Advanced Technology Genomics Core at MD Anderson Cancer Center. Sample concentration and cell suspension viability were evaluated using a Countess II FL Automated Cell Counter (Thermo Fisher Scientific). Samples were normalized for input onto the Chromium Single Cell A Chip Kit (10X Genomics), and single cells were lysed and barcoded for reverse transcription. Equal amounts of each uniquely indexed sample library were pooled together. Pooled libraries were sequenced using a NovaSeq6000 SP 100-cycle flow cell (Illumina). After sequencing, raw reads were aligned to the human genome (hg38), and the digital expression matrix was generated using cellranger count. Individual samples were merged to generate the digital expression matrix using cellranger aggr. The Seurat package in R was used to analyze the digital expression matrix. Cells with less than 100 genes and less than 500 unique molecular identifiers detected were not analyzed further. The Seurat function NormalizeData was used to normalize the raw counts. Variable genes were identified using the FindVariableGenes function. The Seurat ScaleData function was used to scale and center expression values in the dataset for dimensional reduction. Default parameters were used for the Seurat functions. When needed, samples were integrated using the Seurat functions FindIntegrationAnchors and IntegrateData. Principal component analysis and Uniform Manifold Approximation and Projection (UMAP) were used to reduce the dimensions of the data, and the first 2 dimensions were used in plots. To cluster the cells and determine the marker genes for each cluster, we used the FindClusters and FindAllMarkers functions, respectively. Differential expression analysis of the samples was performed using the FindMarkers function and the Wilcoxon rank-sum test. The Benjamini-Hochberg procedure was applied to adjust the false discovery rate. Functional enrichment analysis was performed using the Metascape software (https://metascape.org/gp/index.html#/main/step1).[59] The human hallmark gene set was used. Analyses were performed using gene annotation available in 2020–2023.

CellphoneDB (v2.0.0)[17] was used to analyze the ligand–receptor interactions. Briefly, each cell type was separated by disease classification, and a separate run was performed for each disease classification. The connectome web was plotted using the igraph package in R.

scATAC-seq analysis and bioinformatic pipeline

ScATAC-seq analysis was performed as we described previously.[58] The scATAC-seq Low Cell Input Nuclei Isolation protocol (10X Genomics) was used to isolate nuclei from FACS-purified cells. Extracted nuclei were used for the consecutive steps of the scATAC-seq library preparation protocol following 10X Genomics guidelines. Equal molar concentrations of uniquely indexed samples were pooled together. Pooled libraries were sequenced using a NextSeq500 150-cycle flow cell (Illumina). Reads were aligned to human (hg38) genomes, and peaks were called using the cellranger-atac count pipeline. Individual samples were merged using the cellranger-atac pipeline to generate the peak-barcode matrix and TF-barcode matrix. To identify specific TF activity for each cell cluster, we used the R package Seurat to analyze the TF-barcode matrix. The raw counts were normalized by the sequencing depth for each cell and scaled for each TF using the NormalizeData and ScaleData functions. Principal component analysis and UMAP were applied to reduce the dimensions of the data, and the first 2 dimensions were plotted. The FindClusters function was used to cluster the cells. The FindAllMarkers function was used to determine the TF markers for each cluster. Differential analysis of TF activity in the samples was performed using the FindMarkers function and the Wilcoxon rank-sum test. Cluster identity was determined based on the activity of master regulators of lineage commitment, as we[60] and others[33,61] described previously. Cluster-specific peaks were determined using the FindAllMarkers function, and differentially accessible peaks between the samples were determined using the FindMarkers function. Each peak was associated with a specific gene based on its distance to that gene's transcription start site (TSS). Peaks overlapping with a promoter region (−1,000 bp, +100 bp) of any TSS were annotated as peaks in promoters, whereas peaks not in promoter regions but within 200 kb of the closest TSS were annotated as peaks in the distal elements. Peaks not mapped in either the promoters or distal elements were annotated as peaks in intergenic regions.

scDNA and protein-seq analysis

Simultaneous analyses of DNA mutations and the cell-surface immunophenotype (scDNA and protein-seq) were performed as we described previously[62] and according to the Mission Bio protocol using the custom-designed 37-gene myeloid panel kit and 48 oligo-conjugated antibodies against all major BM cell types (Biolegend). Briefly, cryopreserved BM MNCs were thawed, quantified, and then stained with the pool of the oligo-conjugated antibodies. Stained cells were washed and loaded onto the Tapestri machine for single-cell encapsulation, lysis, and barcoding. DNA libraries were extracted from the droplets followed by the purification using Ampure XP beads (Beckman Coulter). Then, the supernatant was incubated with biotinylated oligonucleotides (Integrated DNA Technologies) to capture the antibody tags, followed by purification using streptavidin beads (Thermo Fisher Scientific). Purified DNA and antibody-tagged libraries were indexed and then sequenced on the Illumina NovaSeq 6000 or NextSeq 500 systems with 150 bp paired-end multiplexed runs.

The resulting files containing DNA and protein data were visualized using the Mission Bio Mosaic library version 1.8. Only manually curated and whitelisted variants were used. Variants were filtered using the below setting: min_dp = 5, min_gq = 0, min_vaf = 21, max_vaf = 100, min_prct_cells = 0, min_mut_prct_cells = 0, and min_std = 0. Protein reads were normalized by centered log ratio, and subsequently underwent dimensionality reduction and clustering using Mosaic 'run_pca' (components = 15), 'run_umap' (attribute = 'pca', n_neighbors = 20, metric = 'cosine', min_dist = 0), and 'cluster' (attribute = 'umap', method = 'graph-community', k = 150). Default parameters were used unless otherwise specified, and randomness was controlled in all steps. Heatmaps were separately visualized in R using the ComplexHeatmap package (https://bioconductor.org/packages/release/bioc/html/ComplexHeatmap.html).

Primary cell culture assays

FACS-purified $\text{Lin}^-\text{CD34}^+$ HSPCs were resuspended in cytokine-free sterile RPMI medium supplemented with 10% FBS, 1% penicillin-streptomycin, and 0.1% amphotericin B and plated in 48-well plates previously seeded with low-passage ($p \leq 4$) healthy BM-derived human mesenchymal cells. Co-cultures were incubated at 37°C in a 5% CO_2 atmosphere. After treatment with vehicle or AMG-176 (20 nM) for 48 h, cells were harvested and stained for quantitative flow cytometric analysis using the antibody panel described above and with AccuCheck Counting Beads (Thermo Fisher Scientific) added to each tube.

QUANTIFICATION AND STATISTICAL ANALYSIS

Statistical analysis of flow cytometry data was performed using Prism 8 software (https://www.graphpad.com). The figure legends include the statistical test(s) used in each experiment. Statistical significance was represented as $^*p < 0.05$, $^{**}p < 0.01$, $^{***}p < 0.001$, and $^{****}p < 0.0001$. In all analyses involving human samples, investigators were blinded to sample annotations and patient outcomes. For replicated experiments, the number of replicates is indicated in the figure legends. No statistical method was used to predetermine the sample size. No data were excluded from the analyses. The experiments were not randomized. Statistical analysis for blast progression and survival in the clinical cohort was performed as specified in the "clinical data analysis" section (method details).

Cell Reports Medicine, Volume *5*

Supplemental information

Targeting MCL1-driven anti-apoptotic pathways overcomes blast progression after hypomethylating agent failure in chronic myelomonocytic leukemia

Guillermo Montalban-Bravo, Natthakan Thongon, Juan Jose Rodriguez-Sevilla, Feiyang Ma, Irene Ganan-Gomez, Hui Yang, Yi June Kim, Vera Adema, Bethany Wildeman, Tomoyuki Tanaka, Faezeh Darbaniyan, Gheath Al-Atrash, Karen Dwyer, Sanam Loghavi, Rashmi Kanagal-Shamanna, Xingzhi Song, Jianhua Zhang, Koichi Takahashi, Hagop Kantarjian, Guillermo Garcia-Manero, and Simona Colla

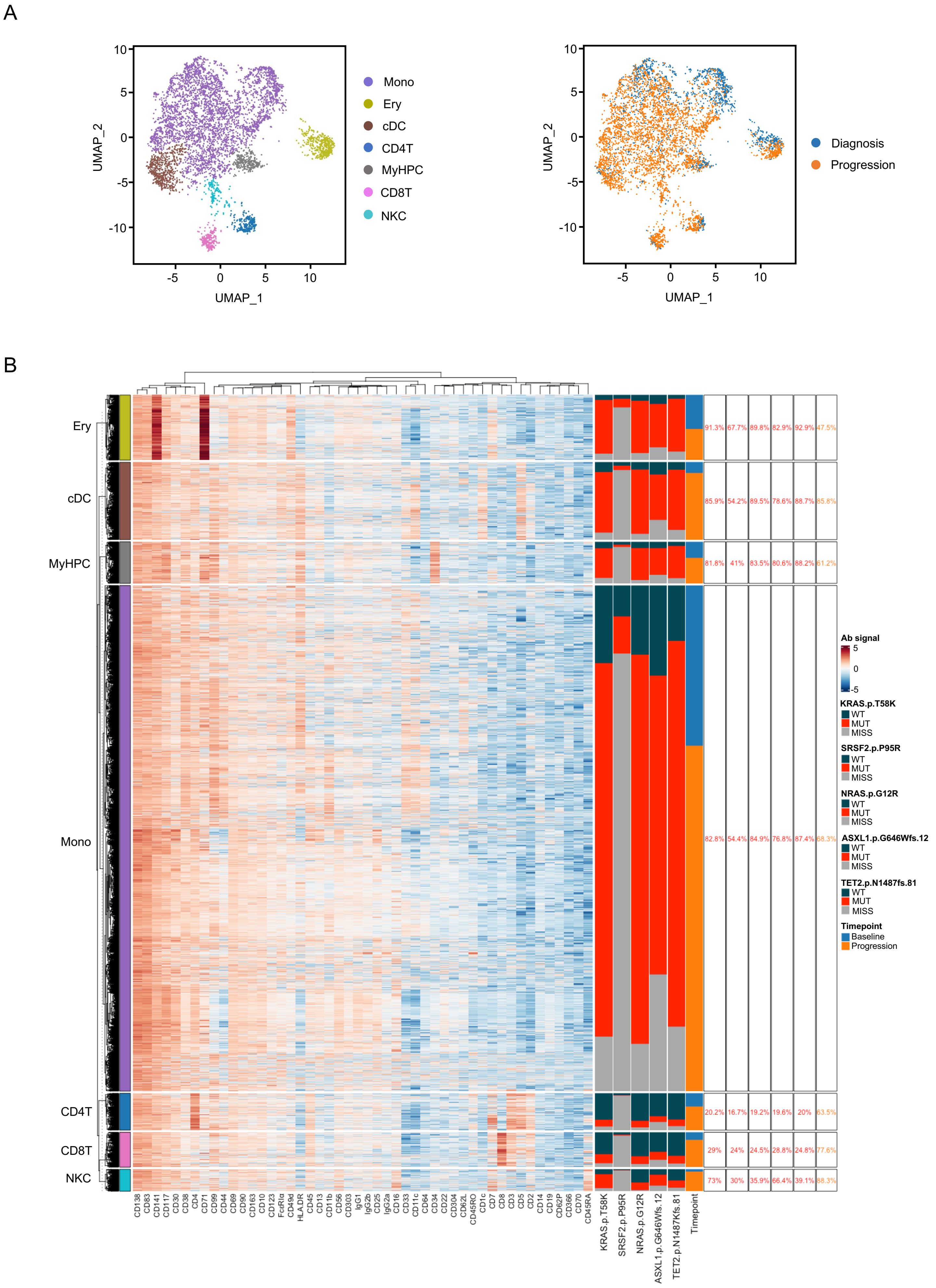
A
UMAP_2
UMAP_1
Mono
Ery
cDC
CD4T
MyHPC
CD8T
NKC
Diagnosis
Progression
B
Ery
cDC
MyHPC
Mono
CD4T
CD8T
NKC
91.3% 67.7% 89.8% 82.9% 92.9% 47.5%
85.9% 54.2% 89.5% 78.6% 88.7% 85.8%
81.8% 41% 83.5% 80.6% 88.2% 61.2%
82.8% 54.4% 84.9% 76.8% 87.4% 68.3%
20.2% 16.7% 19.2% 19.6% 20% 63.5%
29% 24% 24.5% 28.8% 24.8% 77.6%
73% 30% 35.9% 66.4% 39.1% 88.3%
CD138 CD83 CD141 CD117 CD30 CD38 CD4 CD71 CD99 CD44 CD69 CD90 CD163 CD10 CD123 FcεRIα CD49d HLA.DR CD45 CD13 CD11b CD56 CD303 IgG1 IgG2b CD25 IgG2a CD16 CD33 CD11c CD64 CD34 CD304 CD22 CD62L CD45RO CD1c CD7 CD8 CD3 CD5 CD2 CD14 CD19 CD62P CD366 CD70 CD45RA
KRAS.p.T58K
SRSF2.p.P95R
NRAS.p.G12R
ASXL1.p.G646Wfs.12
TET2.p.N1487Kfs.81
Timepoint
Ab signal
5
0
-5
KRAS.p.T58K
WT
MUT
MISS
SRSF2.p.P95R
WT
MUT
MISS
NRAS.p.G12R
WT
MUT
MISS
ASXL1.p.G646Wfs.12
WT
MUT
MISS
TET2.p.N1487fs.81
WT
MUT
MISS
Timepoint
Baseline
Progression

Figure S1. Mutations in *RAS* pathway signaling genes predict a high risk of CMML BP after HMA therapy failure. Related to Figure 1. (A) UMAP of scDNA and protein-seq data for pooled MNCs isolated from BM samples obtained from a CMML patient with pre-existing $KRAS^{T58K}$ and $NRAS^{G12R}$ mutations at diagnosis (n=1,826) and at BP after HMA therapy failure (n=4,001) included in the CMML patient cohort in Figure 1 and evaluated patient samples in Figure 4. BP was not associated with the clonal evolution of these mutations as they both had approximately 50% VAF at the onset of the disease. Each dot represents one cell. Cells are clustered based on immunophenotypic markers. Different colors represent cluster identity (left) or origin (right). Mono, monocytes; Ery, erythroid precursors; cDC, classical dendritic cells; CD4T, $CD4^+$ T cells; MyHPC, myeloid hematopoietic progenitor cells; CD8T, $CD8^+$ T cells; NKC, natural killer cells. **(B)** Heatmap displaying DNA and protein reads from each sequenced cell type shown in Fig. S1A. Colors for protein data correspond to antibody-oligonucleotide intensity signals. High protein expression is depicted in red, and low protein expression is depicted in blue. DNA colors correspond to the genotypes for each individual mutation per cell read (wild-type = dark grey, mutant = red, missing = light grey) based on cluster. Percentages correspond to the frequencies of mutant reads within each cluster for a given mutation.

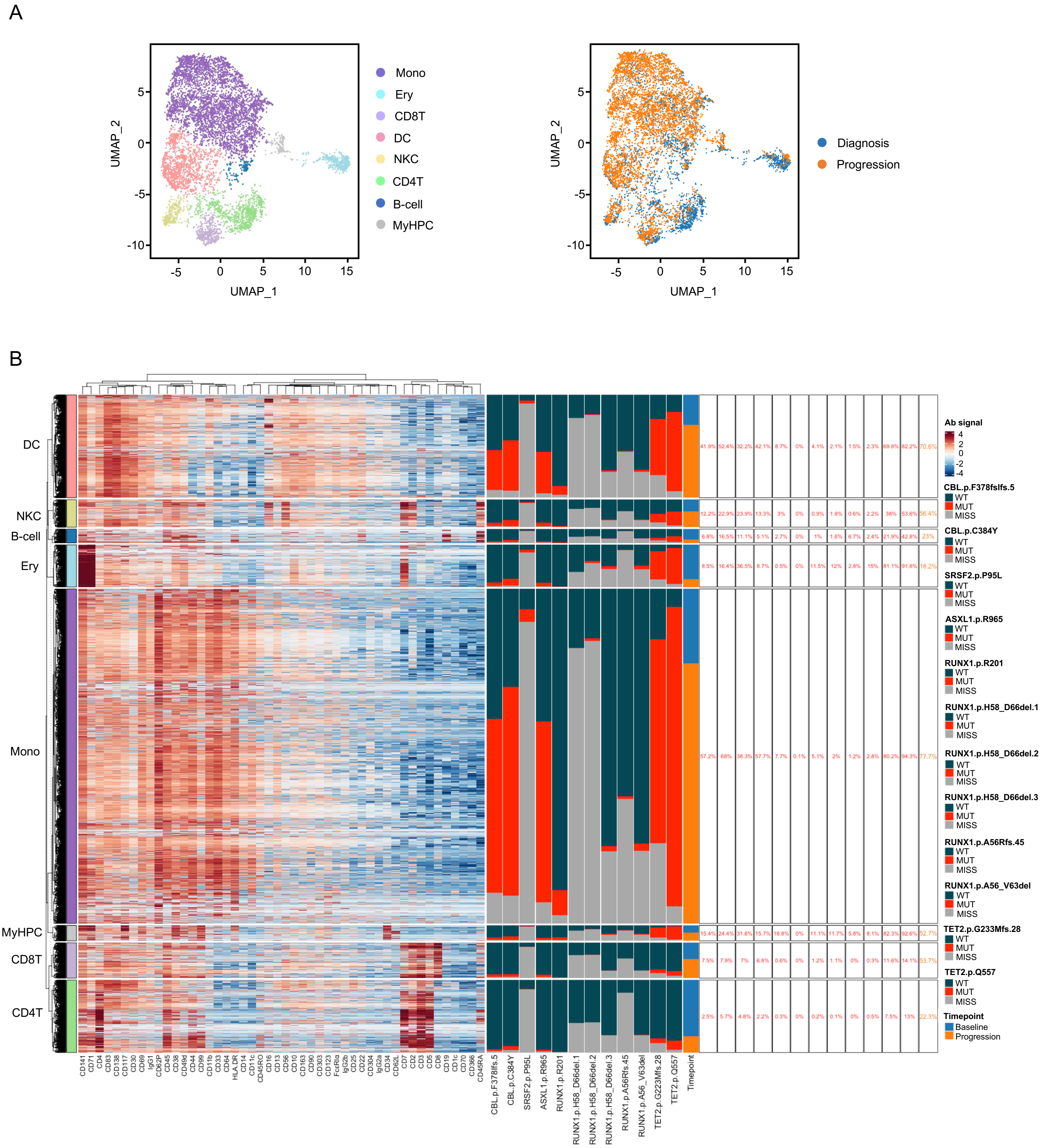
A
UMAP_2
UMAP_1
5
0
-5
-10
-5
0
5
10
15
Mono
Ery
CD8T
DC
NKC
CD4T
B-cell
MyHPC
Diagnosis
Progression
B
DC
NKC
B-cell
Ery
Mono
MyHPC
CD8T
CD4T
CD141
CD71
CD4
CD83
CD138
CD117
CD30
CD69
IgG1
CD62P
CD45
CD38
CD49d
CD44
CD99
CD11b
CD33
CD64
HLA.DR
CD14
CD11c
CD45RO
CD16
CD13
CD56
CD10
CD163
CD90
CD303
CD123
FcεRIα
IgG2b
CD25
CD22
CD304
IgG2a
CD34
CD62L
CD7
CD2
CD3
CD5
CD8
CD19
CD1c
CD70
CD366
CD45RA
CBL.p.F378Ifs.5
CBL.p.C384Y
SRSF2.p.P95L
ASXL1.p.R965
RUNX1.p.R201
RUNX1.p.H58_D66del.1
RUNX1.p.H58_D66del.2
RUNX1.p.H58_D66del.3
RUNX1.p.A56Rfs.45
RUNX1.p.A56_V63del
TET2.p.G233Mfs.28
TET2.p.Q557
Timepoint
41.9% 52.4% 32.2% 42.1% 8.7% 0% 4.1% 2.1% 1.5% 2.3% 69.8% 82.2% 70.6%
12.2% 22.9% 23.9% 13.3% 3% 0% 0.9% 1.8% 0.6% 2.2% 38% 53.6% 56.4%
6.8% 16.5% 11.1% 5.1% 2.7% 0% 1% 1.6% 6.7% 2.4% 21.9% 42.8% 23%
8.5% 16.4% 36.5% 8.7% 0.5% 0% 11.5% 12% 2.8% 15% 81.1% 91.8% 18.2%
57.2% 68% 38.3% 57.7% 7.7% 0.1% 5.1% 2% 1.2% 2.8% 80.2% 94.3% 77.7%
15.4% 24.4% 31.6% 15.7% 18.8% 0% 11.1% 11.7% 5.8% 8.1% 82.3% 92.6% 52.7%
7.5% 7.9% 7% 6.8% 0.6% 0% 1.2% 1.1% 0% 0.3% 11.6% 14.1% 53.7%
2.5% 5.7% 4.8% 2.2% 0.3% 0% 0.2% 0.1% 0% 0.5% 7.5% 13% 22.3%
Ab signal
4
2
0
-2
-4
CBL.p.F378Ifs.5
WT
MUT
MISS
CBL.p.C384Y
WT
MUT
MISS
SRSF2.p.P95L
WT
MUT
MISS
ASXL1.p.R965
WT
MUT
MISS
RUNX1.p.R201
WT
MUT
MISS
RUNX1.p.H58_D66del.1
WT
MUT
MISS
RUNX1.p.H58_D66del.2
WT
MUT
MISS
RUNX1.p.H58_D66del.3
WT
MUT
MISS
RUNX1.p.A56Rfs.45
WT
MUT
MISS
RUNX1.p.A56_V63del
WT
MUT
MISS
TET2.p.G233Mfs.28
WT
MUT
MISS
TET2.p.Q557
WT
MUT
MISS
Timepoint
Baseline
Progression

Figure S2. *RAS* pathway mutant clones expand at BP after HMA therapy failure in CMML. Related to Figure 1. (A) UMAP of scDNA and protein-seq data for pooled MNCs isolated from BM samples obtained from a CMML patient at diagnosis (n=3,213) and at BP after HMA therapy failure (n=5,342) included in the CMML patient cohort in Figure 1 and evaluated patient samples in Figure 4. BP was associated with the clonal evolution of a pre-existing *CBL*^{F378Ifs} mutation and the acquisition of a previously undetected *CBL*^{C384Y} mutation. Each dot represents one cell. Cells are clustered based on immunophenotypic markers. Different colors represent cluster identity (left) or origin (right). Mono, monocytes; Ery, erythroid precursors; CD8T, CD8^{+} T cells; DC, classical dendritic cells; NKC, natural killer cells; CD4T, CD4^{+} T cells; B cell, B lymphocytes, MyHPC; myeloid hematopoietic progenitor cells. **(B)** Heatmap displaying DNA and protein reads from each sequenced cell type as shown in Fig. S2A. Colors for protein data correspond to antibody-oligonucleotide intensity signals. Red indicates high protein expression, and blue indicates low protein expression. Colors for DNA data correspond to the genotype for each individual mutation per cell read (wild-type = dark grey, mutant = red, missing = light grey) based on cluster. Percentages correspond to the frequencies of mutant reads within each cluster for a given mutation.

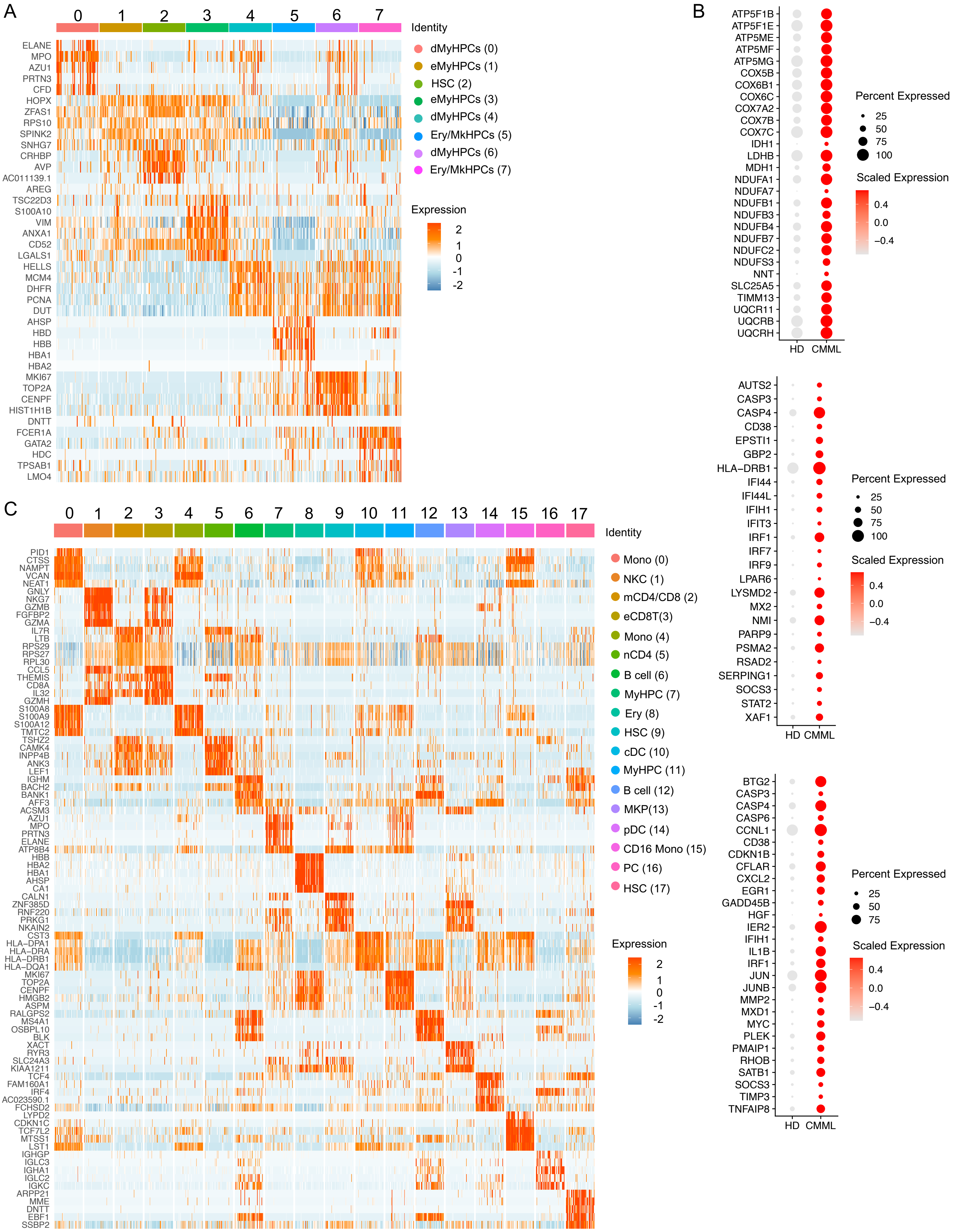
A
0
1
2
3
4
5
6
7
Identity
dMyHPCs (0)
eMyHPCs (1)
HSC (2)
eMyHPCs (3)
dMyHPCs (4)
Ery/MkHPCs (5)
dMyHPCs (6)
Ery/MkHPCs (7)
Expression
2
1
0
-1
-2
ELANE
MPO
AZU1
PRTN3
CFD
HOPX
ZFAS1
RPS10
SPINK2
SNHG7
CRHBP
AVP
AC011139.1
AREG
TSC22D3
S100A10
VIM
ANXA1
CD52
LGALS1
HELLS
MCM4
DHFR
PCNA
DUT
AHSP
HBD
HBB
HBA1
HBA2
MKI67
TOP2A
CENPF
HIST1H1B
DNTT
FCER1A
GATA2
HDC
TPSAB1
LMO4
B
ATP5F1B
ATP5F1E
ATP5ME
ATP5MF
ATP5MG
COX5B
COX6B1
COX6C
COX7A2
COX7B
COX7C
IDH1
LDHB
MDH1
NDUFA1
NDUFA7
NDUFB1
NDUFB3
NDUFB4
NDUFB7
NDUFC2
NDUFS3
NNT
SLC25A5
TIMM13
UQCR11
UQCRB
UQCRH
HD
CMML
Percent Expressed
25
50
75
100
Scaled Expression
0.4
0.0
−0.4
AUTS2
CASP3
CASP4
CD38
EPSTI1
GBP2
HLA−DRB1
IFI44
IFI44L
IFIH1
IFIT3
IRF1
IRF7
IRF9
LPAR6
LYSMD2
MX2
NMI
PARP9
PSMA2
RSAD2
SERPING1
SOCS3
STAT2
XAF1
HD
CMML
Percent Expressed
25
50
75
100
Scaled Expression
0.4
0.0
−0.4
BTG2
CASP3
CASP4
CASP6
CCNL1
CD38
CDKN1B
CFLAR
CXCL2
EGR1
GADD45B
HGF
IER2
IFIH1
IL1B
IRF1
JUN
JUNB
MMP2
MXD1
MYC
PLEK
PMAIP1
RHOB
SATB1
SOCS3
TIMP3
TNFAIP8
HD
CMML
Percent Expressed
25
50
75
Scaled Expression
0.4
0.0
−0.4
C
0
1
2
3
4
5
6
7
8
9
10
11
12
13
14
15
16
17
Identity
Mono (0)
NKC (1)
mCD4/CD8 (2)
eCD8T(3)
Mono (4)
nCD4 (5)
B cell (6)
MyHPC (7)
Ery (8)
HSC (9)
cDC (10)
MyHPC (11)
B cell (12)
MKP(13)
pDC (14)
CD16 Mono (15)
PC (16)
HSC (17)
Expression
2
1
0
-1
-2
PID1
CTSS
NAMPT
VCAN
NEAT1
GNLY
NKG7
GZMB
FGFBP2
GZMA
IL7R
LTB
RPS29
RPS27
RPL30
CCL5
THEMIS
CD8A
IL32
GZMH
S100A8
S100A9
S100A12
TMTC2
TSHZ2
CAMK4
INPP4B
ANK3
LEF1
IGHM
BACH2
BANK1
AFF3
ACSM3
AZU1
MPO
PRTN3
ELANE
ATP8B4
HBB
HBA2
HBA1
AHSP
CA1
CALN1
ZNF385D
RNF220
PRKG1
NKAIN2
CST3
HLA−DPA1
HLA−DRA
HLA−DRB1
HLA−DQA1
MKI67
TOP2A
CENPF
HMGB2
ASPM
RALGPS2
MS4A1
OSBPL10
BLK
XACT
RYR3
SLC24A3
KIAA1211
TCF4
FAM160A1
IRF4
AC023590.1
FCHSD2
LYPD2
CDKN1C
TCF7L2
MTSS1
LST1
IGHGP
IGLC3
IGHA1
IGLC2
IGKC
ARPP21
MME
DNTT
EBF1
SSBP2

Figure S3. *RAS* pathway mutated CMML cells activate cell-intrinsic and -extrinsic inflammatory networks. Related to Figure 2. **(A)** Heatmap of the expression levels of the top 5 genes enriched in each of the 8 clusters shown in Fig. 2A. **(B)** Dot plots of the genes belonging to oxidative phosphorylation (top), IFN response (middle), and apoptosis (bottom) pathways that were significantly overexpressed in the CMML HSCs shown in Fig. 2A compared with those in HD HSCs. The scaled expression represents z scores across conditions. **(C)** Heatmap of the expression levels of the top 5 genes enriched in each of the 18 clusters shown in Fig. 2D.

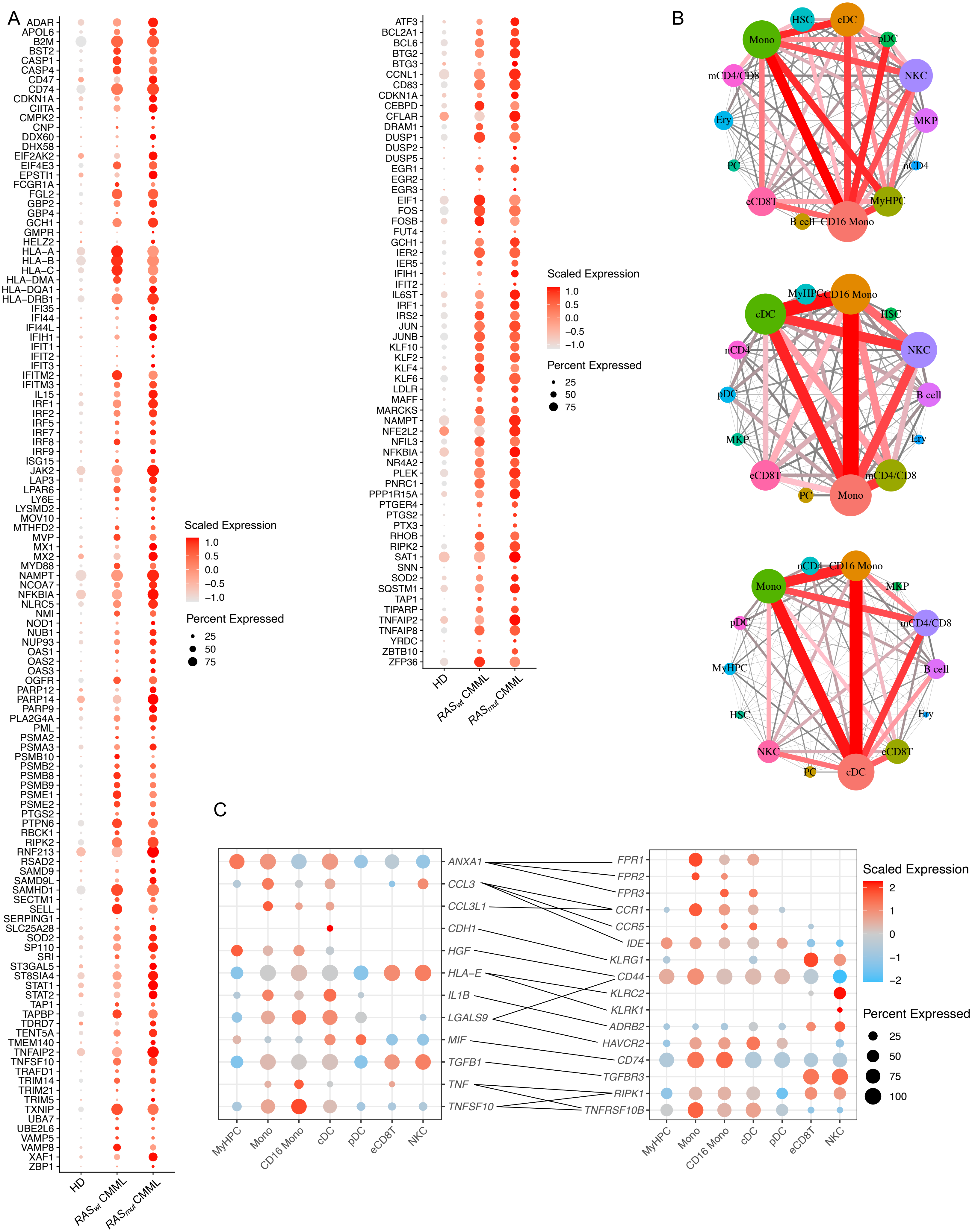
A
ADAR
APOL6
B2M
BST2
CASP1
CASP4
CD47
CD74
CDKN1A
CIITA
CMPK2
CNP
DDX60
DHX58
EIF2AK2
EIF4E3
EPSTI1
FCGR1A
FGL2
GBP2
GBP4
GCH1
GMPR
HELZ2
HLA−A
HLA−B
HLA−C
HLA−DMA
HLA−DQA1
HLA−DRB1
IFI35
IFI44
IFI44L
IFIH1
IFIT1
IFIT2
IFIT3
IFITM2
IFITM3
IL15
IRF1
IRF2
IRF5
IRF7
IRF8
IRF9
ISG15
JAK2
LAP3
LPAR6
LY6E
LYSMD2
MOV10
MTHFD2
MVP
MX1
MX2
MYD88
NAMPT
NCOA7
NFKBIA
NLRC5
NMI
NOD1
NUB1
NUP93
OAS1
OAS2
OAS3
OGFR
PARP12
PARP14
PARP9
PLA2G4A
PML
PSMA2
PSMA3
PSMB10
PSMB2
PSMB8
PSMB9
PSME1
PSME2
PTGS2
PTPN6
RBCK1
RIPK2
RNF213
RSAD2
SAMD9
SAMD9L
SAMHD1
SECTM1
SELL
SERPING1
SLC25A28
SOD2
SP110
SRI
ST3GAL5
ST8SIA4
STAT1
STAT2
TAP1
TAPBP
TDRD7
TENT5A
TMEM140
TNFAIP2
TNFSF10
TRAFD1
TRIM14
TRIM21
TRIM5
TXNIP
UBA7
UBE2L6
VAMP5
VAMP8
XAF1
ZBP1
HD
RAS_{wt} CMML
RAS_{mut} CMML
Scaled Expression
1.0
0.5
0.0
−0.5
−1.0
Percent Expressed
25
50
75
ATF3
BCL2A1
BCL6
BTG2
BTG3
CCNL1
CD83
CDKN1A
CEBPD
CFLAR
DRAM1
DUSP1
DUSP2
DUSP5
EGR1
EGR2
EGR3
EIF1
FOS
FOSB
FUT4
GCH1
IER2
IER5
IFIH1
IFIT2
IL6ST
IRF1
IRS2
JUN
JUNB
KLF10
KLF2
KLF4
KLF6
LDLR
MAFF
MARCKS
NAMPT
NFE2L2
NFIL3
NFKBIA
NR4A2
PLEK
PNRC1
PPP1R15A
PTGER4
PTGS2
PTX3
RHOB
RIPK2
SAT1
SNN
SOD2
SQSTM1
TAP1
TIPARP
TNFAIP2
TNFAIP8
YRDC
ZBTB10
ZFP36
HD
RAS_{wt} CMML
RAS_{mut} CMML
Scaled Expression
1.0
0.5
0.0
−0.5
−1.0
Percent Expressed
25
50
75
B
HSC
cDC
Mono
pDC
mCD4/CD8
NKC
Ery
MKP
PC
nCD4
eCD8T
MyHPC
B cell
CD16 Mono
MyHPC
CD16 Mono
cDC
HSC
nCD4
NKC
pDC
B cell
MKP
Ery
eCD8T
mCD4/CD8
PC
Mono
nCD4
CD16 Mono
Mono
MKP
pDC
mCD4/CD8
MyHPC
B cell
HSC
Ery
NKC
eCD8T
PC
cDC
C
ANXA1
CCL3
CCL3L1
CDH1
HGF
HLA−E
IL1B
LGALS9
MIF
TGFB1
TNF
TNFSF10
FPR1
FPR2
FPR3
CCR1
CCR5
IDE
KLRG1
CD44
KLRC2
KLRK1
ADRB2
HAVCR2
CD74
TGFBR3
RIPK1
TNFRSF10B
MyHPC
Mono
CD16 Mono
cDC
pDC
eCD8T
NKC
MyHPC
Mono
CD16 Mono
cDC
pDC
eCD8T
NKC
Scaled Expression
2
1
0
−1
−2
Percent Expressed
25
50
75
100

Figure S4. *RAS* pathway mutated CMML cells activate inflammatory networks and establish inhibitory immune interactions. Related to Figure 2. **(A)** Dot plots of the genes belonging to IFN response (left) and NF-κB signaling (right) pathways that were significantly overexpressed in *RAS* pathway mutant and/or wild-type CMML monocytes shown in Fig. 2D compared with those in HD monocytes. The scaled expression represents z scores across conditions. **(B)** Connectome web analysis of interactions between BM MNC populations that were significantly increased in *RAS* pathway wild-type (top) or mutant (middle) CMML compared to those of HDs, or in *RAS* pathway mutant CMML compared to *RAS* pathway wild-type CMML (bottom). The vertex (i.e., colored cell node) size is proportional to the number of interactions to and from each cell type, and the thickness of each connecting line is proportional to the number of interactions between 2 nodes. **(C)** Dot plots showing the most significant ligand- (left) to-receptor (right) interactions gained in MNCs from *RAS* pathway mutant CMML patients compared with those from *RAS* pathway wild-type CMML. Lines represent connections between ligands and their corresponding receptors. Color saturation indicates the level of gene expression. Dot size indicates the percentage of each cell type expressing the gene. The scaled expression represents z scores across conditions.

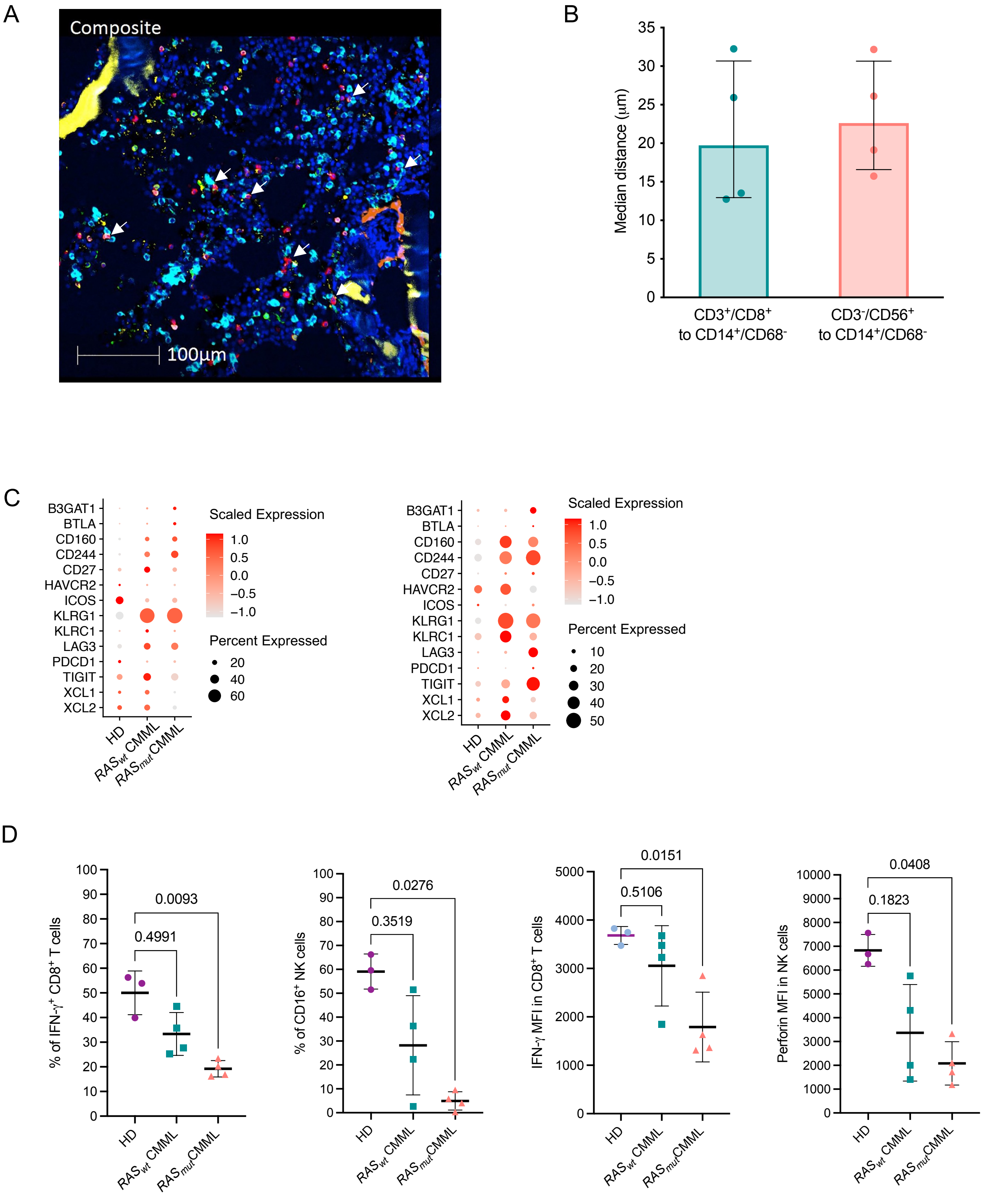
A
Composite
100µm
B
Median distance (µm)
0
5
10
15
20
25
30
35
CD3+/CD8+ to CD14+/CD68-
CD3-/CD56+ to CD14+/CD68-
C
B3GAT1
BTLA
CD160
CD244
CD27
HAVCR2
ICOS
KLRG1
KLRC1
LAG3
PDCD1
TIGIT
XCL1
XCL2
HD
RASwt CMML
RASmut CMML
Scaled Expression
1.0
0.5
0.0
−0.5
−1.0
Percent Expressed
20
40
60
10
30
50
D
% of IFN-γ+ CD8+ T cells
% of CD16+ NK cells
IFN-γ MFI in CD8+ T cells
Perforin MFI in NK cells
0.0093
0.4991
0.0276
0.3519
0.0151
0.5106
0.0408
0.1823
0
1000
2000
3000
4000
5000
6000
7000
8000
9000
10000
HD
RASwt CMML
RASmut CMML

Figure S5. Immune cells are in a dysfunctional state in CMML and spatially co-localize with monocytic populations. Related to Figure 2. (A) Representative multiplex immunofluorescence image of a selected BM section area (20× magnification). Cells were stained with antibodies against CD3 (red), CD4 (green), CD8 (magenta), CD14 (cyan), CD56 (orange), and CD68 (yellow). White arrows indicate the interactions between $CD14^+$ monocytes and $CD3^+$ T cells. **(B)** The median distance between $CD14^+/CD68^-$ monocytes and $CD3^+/CD8^+$ T cells (left) or $CD3^-/CD56^+$ NK cells (right) in BM sections obtained from CMML patients (n=4) at the time of diagnosis. **(C)** Dot plot of exhaustion markers in effector $CD8^+$ T (left) and NK (right) cells from HDs, and *RAS* pathway wild-type (RAS_{wt}) or mutant (RAS_{mut}) CMML. The scaled expression represents z scores across conditions. **(D)** Frequencies of IFN-γ^+ $CD8^+$ T cells (far left), $CD16^+$ NK cells (middle left), and mean fluorescent intensity (MFI) of IFN-γ^+ in $CD8^+$ T cells (middle right) or perforin in NK cells (far right) from the BM of HDs (n=3) and *RAS* pathway wild-type (RAS_{wt}) or mutant (RAS_{mut}) CMML (n=4). Lines represent means. Statistical significance was calculated using the Kruskal-Wallis test.

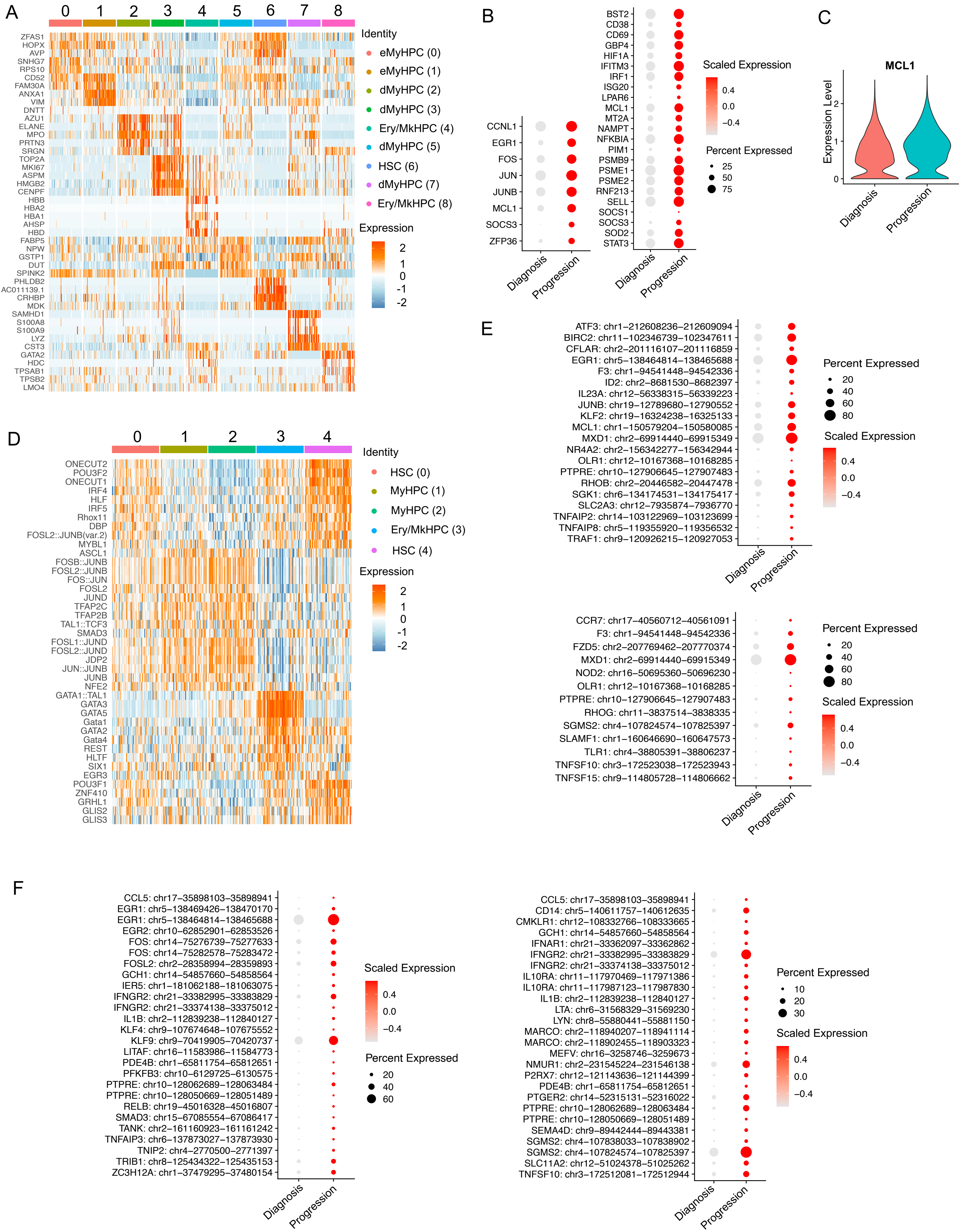
A
0
1
2
3
4
5
6
7
8
ZFAS1
HOPX
AVP
SNHG7
RPS10
CD52
FAM30A
ANXA1
VIM
DNTT
AZU1
ELANE
MPO
PRTN3
SRGN
TOP2A
MKI67
ASPM
HMGB2
CENPF
HBB
HBA2
HBA1
AHSP
HBD
FABP5
NPW
GSTP1
DUT
SPINK2
PHLDB2
AC011139.1
CRHBP
MDK
SAMHD1
S100A8
S100A9
LYZ
CST3
GATA2
HDC
TPSAB1
TPSB2
LMO4
Identity
eMyHPC (0)
eMyHPC (1)
dMyHPC (2)
dMyHPC (3)
Ery/MkHPC (4)
dMyHPC (5)
HSC (6)
dMyHPC (7)
Ery/MkHPC (8)
Expression
2
1
0
-1
-2
B
CCNL1
EGR1
FOS
JUN
JUNB
MCL1
SOCS3
ZFP36
Diagnosis
Progression
BST2
CD38
CD69
GBP4
HIF1A
IFITM3
IRF1
ISG20
LPAR6
MCL1
MT2A
NAMPT
NFKBIA
PIM1
PSMB9
PSME1
PSME2
RNF213
SELL
SOCS1
SOCS3
SOD2
STAT3
Diagnosis
Progression
Scaled Expression
0.4
0.0
−0.4
Percent Expressed
25
50
75
C
MCL1
Expression Level
2
1
0
Diagnosis
Progression
D
0
1
2
3
4
ONECUT2
POU3F2
ONECUT1
IRF4
HLF
IRF5
Rhox11
DBP
FOSL2::JUNB(var.2)
MYBL1
ASCL1
FOSB::JUNB
FOSL2::JUNB
FOS::JUN
FOSL2
JUND
TFAP2C
TFAP2B
TAL1::TCF3
SMAD3
FOSL1::JUND
FOSL2::JUND
JDP2
JUN::JUNB
JUNB
NFE2
GATA1::TAL1
GATA3
GATA5
Gata1
GATA2
Gata4
REST
HLTF
SIX1
EGR3
POU3F1
ZNF410
GRHL1
GLIS2
GLIS3
Identity
HSC (0)
MyHPC (1)
MyHPC (2)
Ery/MkHPC (3)
HSC (4)
Expression
2
1
0
-1
-2
E
ATF3: chr1−212608236−212609094
BIRC2: chr11−102346739−102347611
CFLAR: chr2−201116107−201116859
EGR1: chr5−138464814−138465688
F3: chr1−94541448−94542336
ID2: chr2−8681530−8682397
IL23A: chr12−56338315−56339223
JUNB: chr19−12789680−12790552
KLF2: chr19−16324238−16325133
MCL1: chr1−150579204−150580085
MXD1: chr2−69914440−69915349
NR4A2: chr2−156342277−156342944
OLR1: chr12−10167368−10168285
PTPRE: chr10−127906645−127907483
RHOB: chr2−20446582−20447478
SGK1: chr6−134174531−134175417
SLC2A3: chr12−7935874−7936770
TNFAIP2: chr14−103122969−103123699
TNFAIP8: chr5−119355920−119356532
TRAF1: chr9−120926215−120927053
Diagnosis
Progression
Percent Expressed
20
40
60
80
Scaled Expression
0.4
0.0
−0.4
CCR7: chr17−40560712−40561091
F3: chr1−94541448−94542336
FZD5: chr2−207769462−207770374
MXD1: chr2−69914440−69915349
NOD2: chr16−50695360−50696230
OLR1: chr12−10167368−10168285
PTPRE: chr10−127906645−127907483
RHOG: chr11−3837514−3838335
SGMS2: chr4−107824574−107825397
SLAMF1: chr1−160646690−160647573
TLR1: chr4−38805391−38806237
TNFSF10: chr3−172523038−172523943
TNFSF15: chr9−114805728−114806662
Diagnosis
Progression
Percent Expressed
20
40
60
80
Scaled Expression
0.4
0.0
−0.4
F
CCL5: chr17−35898103−35898941
EGR1: chr5−138469426−138470170
EGR1: chr5−138464814−138465688
EGR2: chr10−62852901−62853526
FOS: chr14−75276739−75277633
FOS: chr14−75282578−75283472
FOSL2: chr2−28358994−28359893
GCH1: chr14−54857660−54858564
IER5: chr1−181062188−181063075
IFNGR2: chr21−33382995−33383829
IFNGR2: chr21−33374138−33375012
IL1B: chr2−112839238−112840127
KLF4: chr9−107674648−107675552
KLF9: chr9−70419905−70420737
LITAF: chr16−11583986−11584773
PDE4B: chr1−65811754−65812651
PFKFB3: chr10−6129725−6130575
PTPRE: chr10−128062689−128063484
PTPRE: chr10−128050669−128051489
RELB: chr19−45016328−45016807
SMAD3: chr15−67085554−67086417
TANK: chr2−161160923−161161242
TNFAIP3: chr6−137873027−137873930
TNIP2: chr4−2770500−2771397
TRIB1: chr8−125434322−125435153
ZC3H12A: chr1−37479295−37480154
Diagnosis
Progression
Scaled Expression
0.4
0.0
−0.4
Percent Expressed
20
40
60
CCL5: chr17−35898103−35898941
CD14: chr5−140611757−140612635
CMKLR1: chr12−108332766−108333665
GCH1: chr14−54857660−54858564
IFNAR1: chr21−33362097−33362862
IFNGR2: chr21−33382995−33383829
IFNGR2: chr21−33374138−33375012
IL10RA: chr11−117970469−117971386
IL10RA: chr11−117987123−117987830
IL1B: chr2−112839238−112840127
LTA: chr6−31568329−31569230
LYN: chr8−55880441−55881150
MARCO: chr2−118940207−118941114
MARCO: chr2−118902455−118903323
MEFV: chr16−3258746−3259673
NMUR1: chr2−231545224−231546138
P2RX7: chr12−121143636−121144399
PDE4B: chr1−65811754−65812651
PTGER2: chr14−52315131−52316022
PTPRE: chr10−128062689−128063484
PTPRE: chr10−128050669−128051489
SEMA4D: chr9−89442444−89443381
SGMS2: chr4−107838033−107838902
SGMS2: chr4−107824574−107825397
SLC11A2: chr12−51024378−51025262
TNFSF10: chr3−172512081−172512944
Diagnosis
Progression
Percent Expressed
10
20
30
Scaled Expression
0.4
0.0
−0.4

Figure S6. *RAS* pathway–mutated HSCs undergo epigenetic reprogramming and drive CMML BP after HMA therapy failure. Related to Figure 3. (A) Heatmap of the expression levels of the top 5 genes enriched in each of the 9 clusters shown in Fig. 3A. **(B)** Dot plots of genes belonging to the NF-κB signaling pathway that were significantly upregulated in *RAS* mutant CMML HSCs (left) and eMyHPCs (right) at BP compared with those at diagnosis (adjusted $P \leq 0.05$). The scaled expression represents z scores across conditions. **(C)** Violin plots of *MCL1* expression levels of *RAS* pathway mutant CMML HSCs at diagnosis and BP (adjusted $P = 2.55 \times 10^{-4}$). **(D)** Heatmap of the activity of the top 10 TFs enriched in each of the 5 clusters shown in Fig. 3D. **(E)** Dot plots of genes involved in the NF-$_{\kappa}$B signaling (top) or inflammatory response (bottom) pathways whose promoters had increased open chromatin peaks in CMML HSCs at BP compared with those at diagnosis ($P \leq 10^{-4}$). The scaled expression represents z scores across conditions. **(F)** Dot plots of genes involved in the NF-$_{\kappa}$B signaling (left) or inflammatory response (right) pathways whose distal regulatory elements had increased open chromatin peaks in CMML HSCs at BP compared with those at diagnosis (adjusted $P \leq 0.05$). The scaled expression represents z scores across conditions.

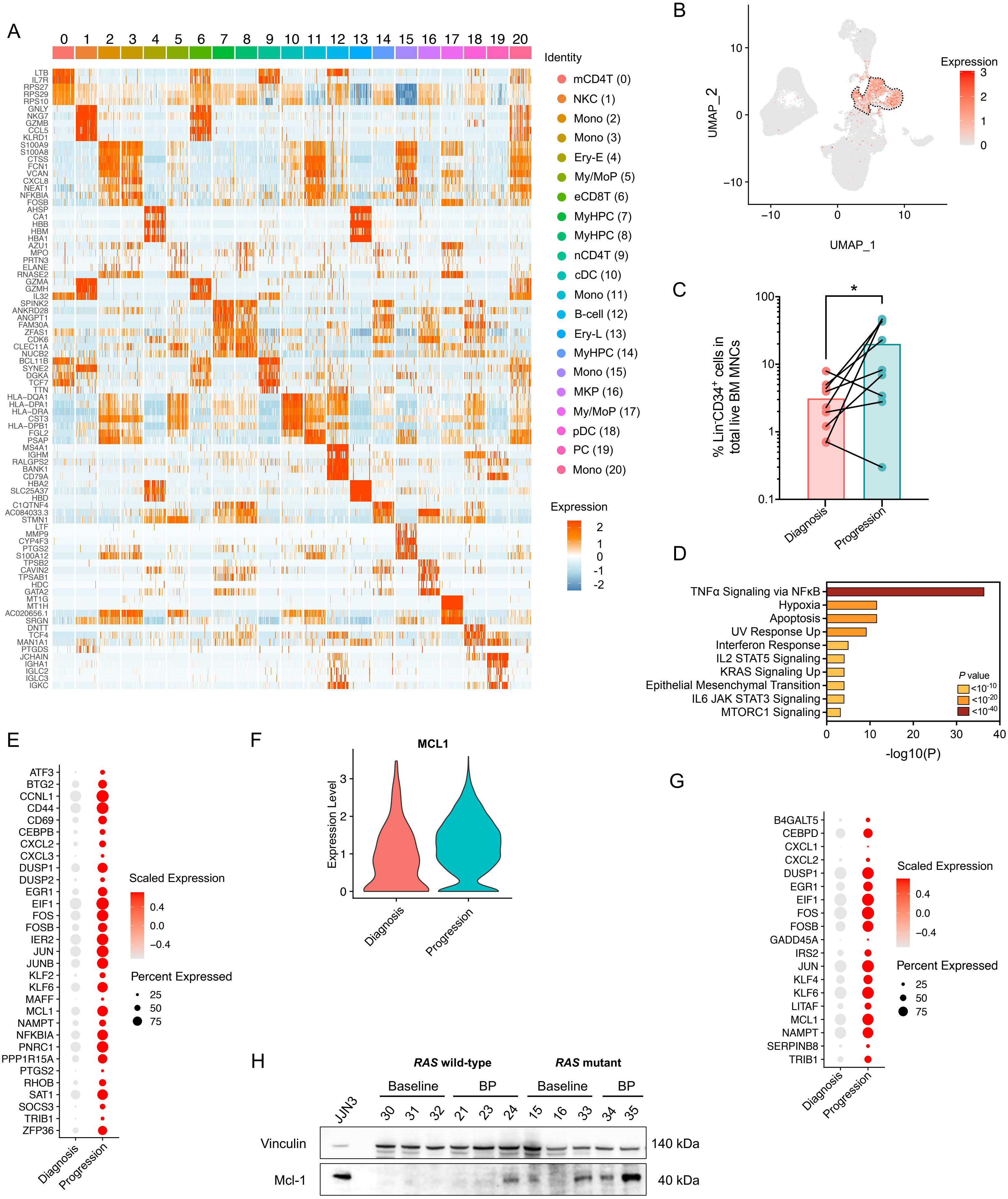
A
0 1 2 3 4 5 6 7 8 9 10 11 12 13 14 15 16 17 18 19 20
LTB
IL7R
RPS27
RPS29
RPS10
GNLY
NKG7
GZMB
CCL5
KLRD1
S100A9
S100A8
CTSS
FCN1
VCAN
CXCL8
NEAT1
NFKBIA
FOSB
AHSP
CA1
HBB
HBM
HBA1
AZU1
MPO
PRTN3
ELANE
RNASE2
GZMA
GZMH
IL32
SPINK2
ANKRD28
ANGPT1
FAM30A
ZFAS1
CDK6
CLEC11A
NUCB2
BCL11B
SYNE2
DGKA
TCF7
TTN
HLA−DQA1
HLA−DPA1
HLA−DRA
CST3
HLA−DPB1
FGL2
PSAP
MS4A1
IGHM
RALGPS2
BANK1
CD79A
HBA2
SLC25A37
HBD
C1QTNF4
AC084033.3
STMN1
LTF
MMP9
CYP4F3
PTGS2
S100A12
TPSB2
CAVIN2
TPSAB1
HDC
GATA2
MT1G
MT1H
AC020656.1
SRGN
DNTT
TCF4
MAN1A1
PTGDS
JCHAIN
IGHA1
IGLC2
IGLC3
IGKC
Identity
mCD4T (0)
NKC (1)
Mono (2)
Mono (3)
Ery-E (4)
My/MoP (5)
eCD8T (6)
MyHPC (7)
MyHPC (8)
nCD4T (9)
cDC (10)
Mono (11)
B-cell (12)
Ery-L (13)
MyHPC (14)
Mono (15)
MKP (16)
My/MoP (17)
pDC (18)
PC (19)
Mono (20)
Expression
2
1
0
-1
-2
B
UMAP_2
UMAP_1
10
0
−10
−10
0
10
Expression
3
2
1
0
C
*
% Lin⁻CD34⁺ cells in total live BM MNCs
100
10
1
0.1
Diagnosis
Progression
D
TNFα Signaling via NFκB
Hypoxia
Apoptosis
UV Response Up
Interferon Response
IL2 STAT5 Signaling
KRAS Signaling Up
Epithelial Mesenchymal Transition
IL6 JAK STAT3 Signaling
MTORC1 Signaling
P value
<10⁻¹⁰
<10⁻²⁰
<10⁻⁴⁰
0
10
20
30
40
-log10(P)
E
ATF3
BTG2
CCNL1
CD44
CD69
CEBPB
CXCL2
CXCL3
DUSP1
DUSP2
EGR1
EIF1
FOS
FOSB
IER2
JUN
JUNB
KLF2
KLF6
MAFF
MCL1
NAMPT
NFKBIA
PNRC1
PPP1R15A
PTGS2
RHOB
SAT1
SOCS3
TRIB1
ZFP36
Diagnosis
Progression
Scaled Expression
0.4
0.0
−0.4
Percent Expressed
25
50
75
F
MCL1
Expression Level
3
2
1
0
Diagnosis
Progression
G
B4GALT5
CEBPD
CXCL1
CXCL2
DUSP1
EGR1
EIF1
FOS
FOSB
GADD45A
IRS2
JUN
KLF4
KLF6
LITAF
MCL1
NAMPT
SERPINB8
TRIB1
Diagnosis
Progression
Scaled Expression
0.4
0.0
−0.4
Percent Expressed
25
50
75
H
RAS wild-type
RAS mutant
Baseline
BP
Baseline
BP
JJN3
30
31
32
21
23
24
15
16
33
34
35
Vinculin
140 kDa
Mcl-1
40 kDa

Figure S7. ***RAS*** **pathway mutated CMML cells upregulate NF-κB survival pathways, including** ***MCL1*****, at BP. Related to Figure 4. (A)** Heatmap of the expression levels of the top 5 genes enriched in each of the 21 clusters shown in Fig. 4A. **(B)** UMAP of the distribution of CD34 expression levels across the clusters, as shown in Fig. 4A. Red shading indicates normalized gene expression. Dashed lines indicate MyHPCs. **(C)** Frequency of Lin$^-$CD34$^+$ cells in MNCs from *RAS* mutant CMML BM samples sequentially collected at diagnosis and BP after HMA therapy failure (n=9). Statistical significance was calculated using a paired two-tailed Student's t-test (*$P < 0.05$). **(D)** Pathway enrichment analysis of the genes that were significantly upregulated in *RAS* mutant MyHPCs at the time of BP compared with those at diagnosis (adjusted $P \leq 0.05$). The top 10 hallmark gene sets are shown. **(E)** Dot plots of genes belonging to the NF-κB signaling pathway that were significantly upregulated in CMML MyHPCs at BP compared with those at diagnosis (adjusted $P \leq 0.05$). The scaled expression represents z scores across conditions. **(F)** Violin plots of *MCL1* expression levels of *RAS* pathway mutant CMML MyHPCs at diagnosis and BP (adjusted $P = 1.12 \times 10^{-15}$). **(G)** Dot plots of genes belonging to the NF-κB signaling pathway that were significantly upregulated in *RAS* pathway mutant CMML monocytes at BP compared with those at diagnosis (adjusted $P \leq 0.05$). The scaled expression represents z scores across conditions. **(H)** Western blot analysis of MCL1 expression levels in CD34$^+$ BM cells isolated from CMML patients at baseline (*RAS* pathway wild-type, n=3; *RAS* pathway mutant, n=3) or at BP (*RAS* pathway wild-type, n=3; *RAS* pathway mutant, n=2). Vinculin was used as a loading control. JJN3 cells are shown as positive controls. The numbers above each case correspond to the patient's UPN (as detailed in Supplementary Table S3).

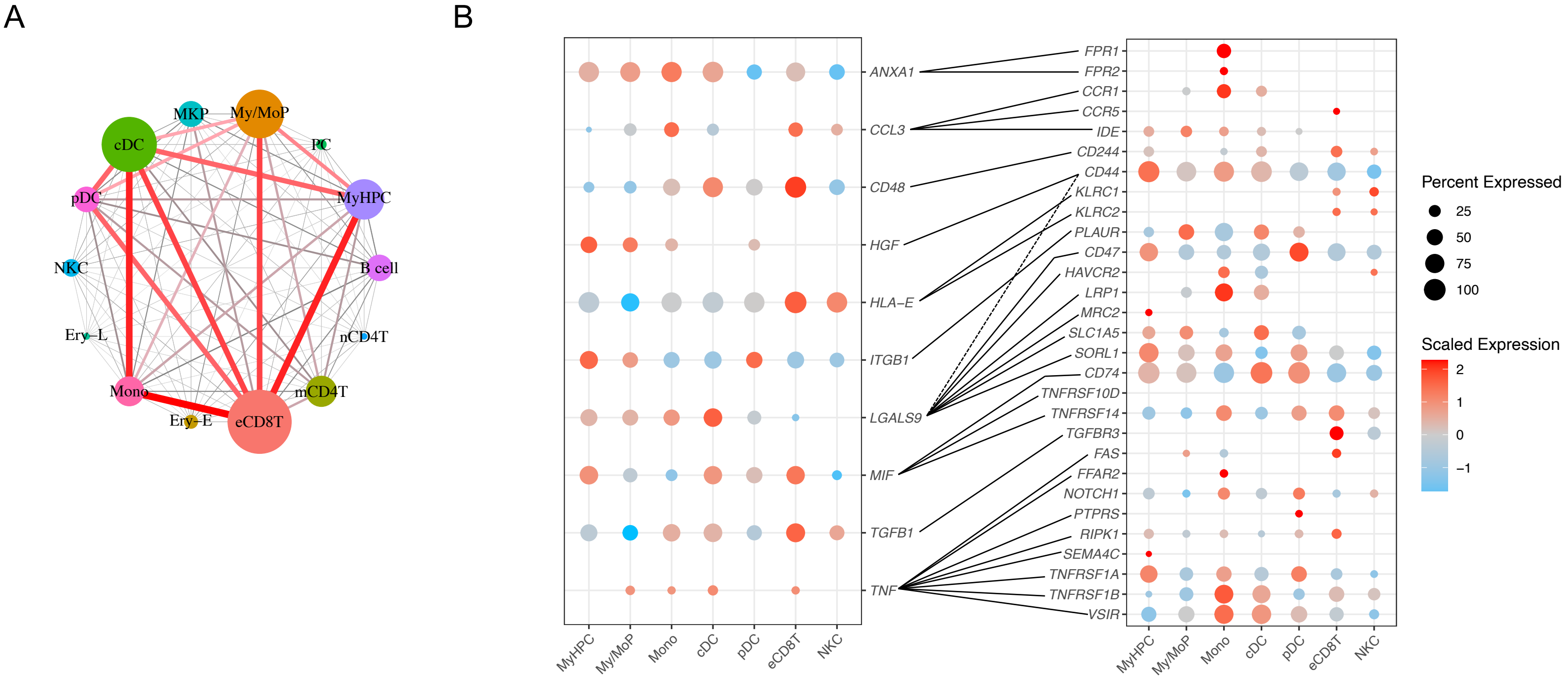

Figure S8. *RAS* pathway mutated CMML MNCs at BP exacerbate the cellular communication networks observed at the time of diagnosis . Related to Figure 4. (A) Connectome web analysis of interactions that were significantly increased in BM MNCs from *RAS* pathway mutant CMML patients at BP compared to those at the time of diagnosis. The vertex (i.e., colored cell node) size is proportional to the number of interactions to and from each cell type, and the thickness of each connecting line is proportional to the number of interactions between 2 nodes. **(B)** Dot plots showing the most significant ligand- (left) to-receptor (right) interactions that were gained in MNCs from *RAS* pathway mutant CMML at diagnosis compared with those at BP (adjusted $P \leq 0.05$). Lines represent connections between ligands and their corresponding receptors. Color saturation indicates the level of gene expression. Dot size indicates the percentage of each cell type expressing the gene. The scaled expression represents z scores across conditions.

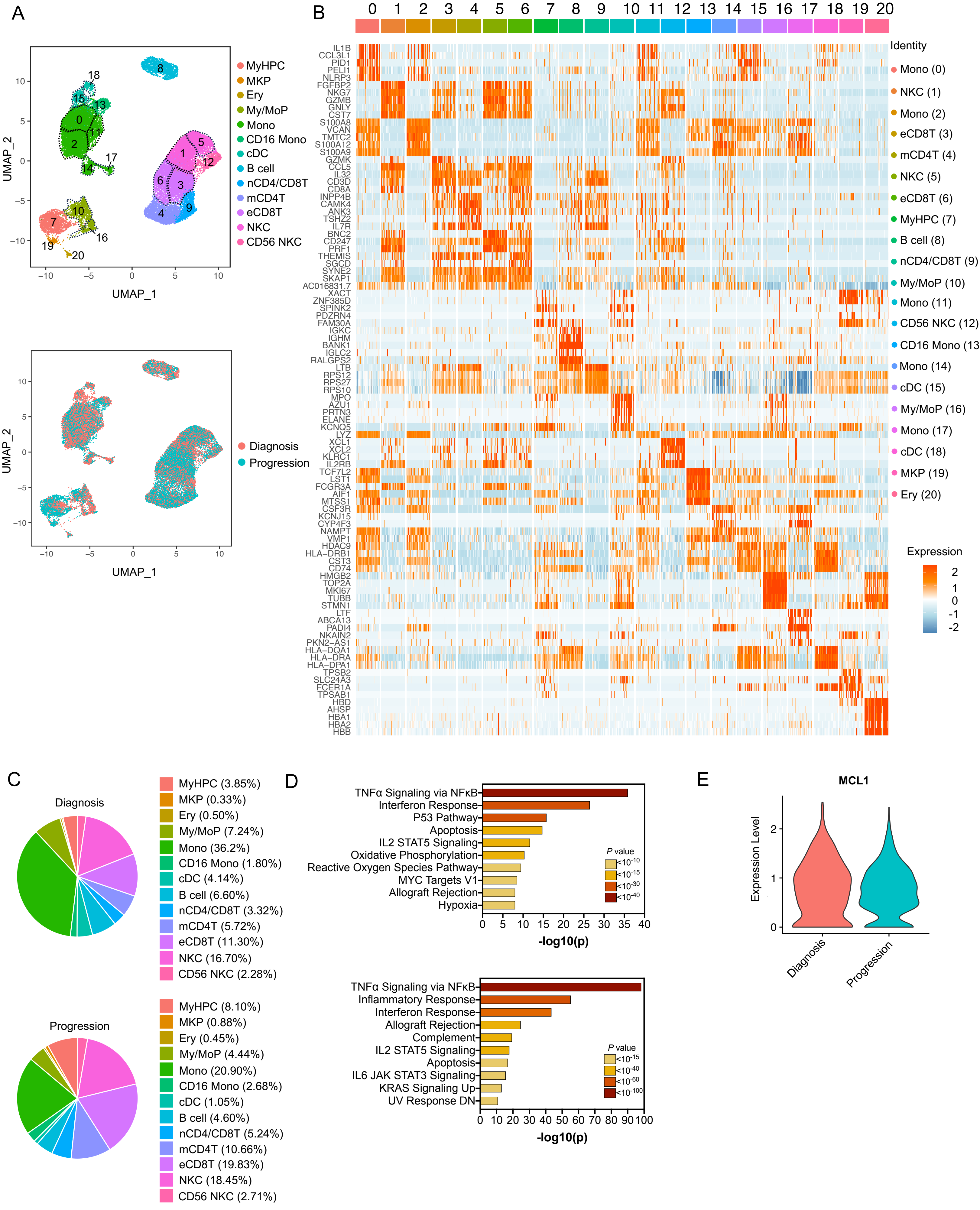
A
UMAP_2
UMAP_1
10
5
0
−5
−10
−10
−5
0
5
10
0
1
2
3
4
5
6
7
8
9
10
11
12
13
14
15
16
17
18
19
20
MyHPC
MKP
Ery
My/MoP
Mono
CD16 Mono
cDC
B cell
nCD4/CD8T
mCD4T
eCD8T
NKC
CD56 NKC
Diagnosis
Progression
B
0 1 2 3 4 5 6 7 8 9 10 11 12 13 14 15 16 17 18 19 20
IL1B
CCL3L1
PID1
PELI1
NLRP3
FGFBP2
NKG7
GZMB
GNLY
CST7
S100A8
VCAN
TMTC2
S100A12
S100A9
GZMK
CCL5
IL32
CD3D
CD8A
INPP4B
CAMK4
ANK3
TSHZ2
IL7R
BNC2
CD247
PRF1
THEMIS
SGCD
SYNE2
SKAP1
AC016831.7
XACT
ZNF385D
SPINK2
PDZRN4
FAM30A
IGKC
IGHM
BANK1
IGLC2
RALGPS2
LTB
RPS12
RPS27
RPS10
MPO
AZU1
PRTN3
ELANE
KCNQ5
LYZ
XCL1
XCL2
KLRC1
IL2RB
TCF7L2
LST1
FCGR3A
AIF1
MTSS1
CSF3R
KCNJ15
CYP4F3
NAMPT
VMP1
HDAC9
HLA−DRB1
CST3
CD74
HMGB2
TOP2A
MKI67
TUBB
STMN1
LTF
ABCA13
PADI4
NKAIN2
PKN2−AS1
HLA−DQA1
HLA−DRA
HLA−DPA1
TPSB2
SLC24A3
FCER1A
TPSAB1
HBD
AHSP
HBA1
HBA2
HBB
Identity
Mono (0)
NKC (1)
Mono (2)
eCD8T (3)
mCD4T (4)
NKC (5)
eCD8T (6)
MyHPC (7)
B cell (8)
nCD4/CD8T (9)
My/MoP (10)
Mono (11)
CD56 NKC (12)
CD16 Mono (13
Mono (14)
cDC (15)
My/MoP (16)
Mono (17)
cDC (18)
MKP (19)
Ery (20)
Expression
2
1
0
-1
-2
C
Diagnosis
MyHPC (3.85%)
MKP (0.33%)
Ery (0.50%)
My/MoP (7.24%)
Mono (36.2%)
CD16 Mono (1.80%)
cDC (4.14%)
B cell (6.60%)
nCD4/CD8T (3.32%)
mCD4T (5.72%)
eCD8T (11.30%)
NKC (16.70%)
CD56 NKC (2.28%)
Progression
MyHPC (8.10%)
MKP (0.88%)
Ery (0.45%)
My/MoP (4.44%)
Mono (20.90%)
CD16 Mono (2.68%)
cDC (1.05%)
B cell (4.60%)
nCD4/CD8T (5.24%)
mCD4T (10.66%)
eCD8T (19.83%)
NKC (18.45%)
CD56 NKC (2.71%)
D
TNFα Signaling via NFκB
Interferon Response
P53 Pathway
Apoptosis
IL2 STAT5 Signaling
Oxidative Phosphorylation
Reactive Oxygen Species Pathway
MYC Targets V1
Allograft Rejection
Hypoxia
P value
<10-10
<10-15
<10-30
<10-40
0 5 10 15 20 25 30 35 40
-log10(p)
TNFα Signaling via NFκB
Inflammatory Response
Interferon Response
Allograft Rejection
Complement
IL2 STAT5 Signaling
Apoptosis
IL6 JAK STAT3 Signaling
KRAS Signaling Up
UV Response DN
P value
<10-15
<10-40
<10-60
<10-100
0 10 20 30 40 50 60 70 80 90 100
-log10(p)
E
MCL1
Expression Level
2
1
0
Diagnosis
Progression

Figure S9. *RAS* pathway wildtype CMML cells do not upregulate MCL1-driven antiapoptotic responses at BP. Related to Figure 4. **(A)** UMAP of scRNA-seq data for pooled single MNCs isolated from 3 BM samples isolated from *RAS* pathway wild-type CMML patients at diagnosis (n=16,070) and BP after HMA therapy failure (n=17,747). Each dot represents one cell. Different colors represent the cluster cell type identity (top) or sample origin (bottom). MyHPC, myeloid hematopoietic progenitor cells; MKP, megakaryocytic progenitor cells; Ery, erythroid precursors; My/MoP, myelo/monocytic progenitors; Mono, monocytes; CD16 Mono, $CD16^+$ non-classical monocytes; cDC, classical dendritic cells; B cell, B lymphocytes; nCD4/CD8T, naïve $CD4^{+,}$ and $CD8^+$ T cells; mCD4T, memory $CD4^+$ T cells; eCD8T, effector $CD8^+$ T cells; NKC, natural killer cells; CD56 NKC, $CD56^+$ natural killer cells. Dashed lines indicate single clusters in each cell type population. **(B)** Heatmap of the expression levels of the top 5 genes enriched in each of the 21 clusters shown in Supplementary Fig. S9A. **(C)** Distribution of MNC populations at diagnosis (top) and BP (bottom) among the clusters shown in Fig. S9A. **(D)** Pathway enrichment analysis of the genes that were significantly upregulated in MyHPCs (top) and monocytes (bottom) from *RAS* pathway wild-type CMML at the time of BP compared with those at diagnosis (adjusted $P \leq 0.05$). The top 10 hallmark gene sets are shown. **(E)** Violin plots of *MCL1* expression levels in *RAS* pathway wild-type CMML MyHPCs at diagnosis and BP (adjusted P = no significant differences).

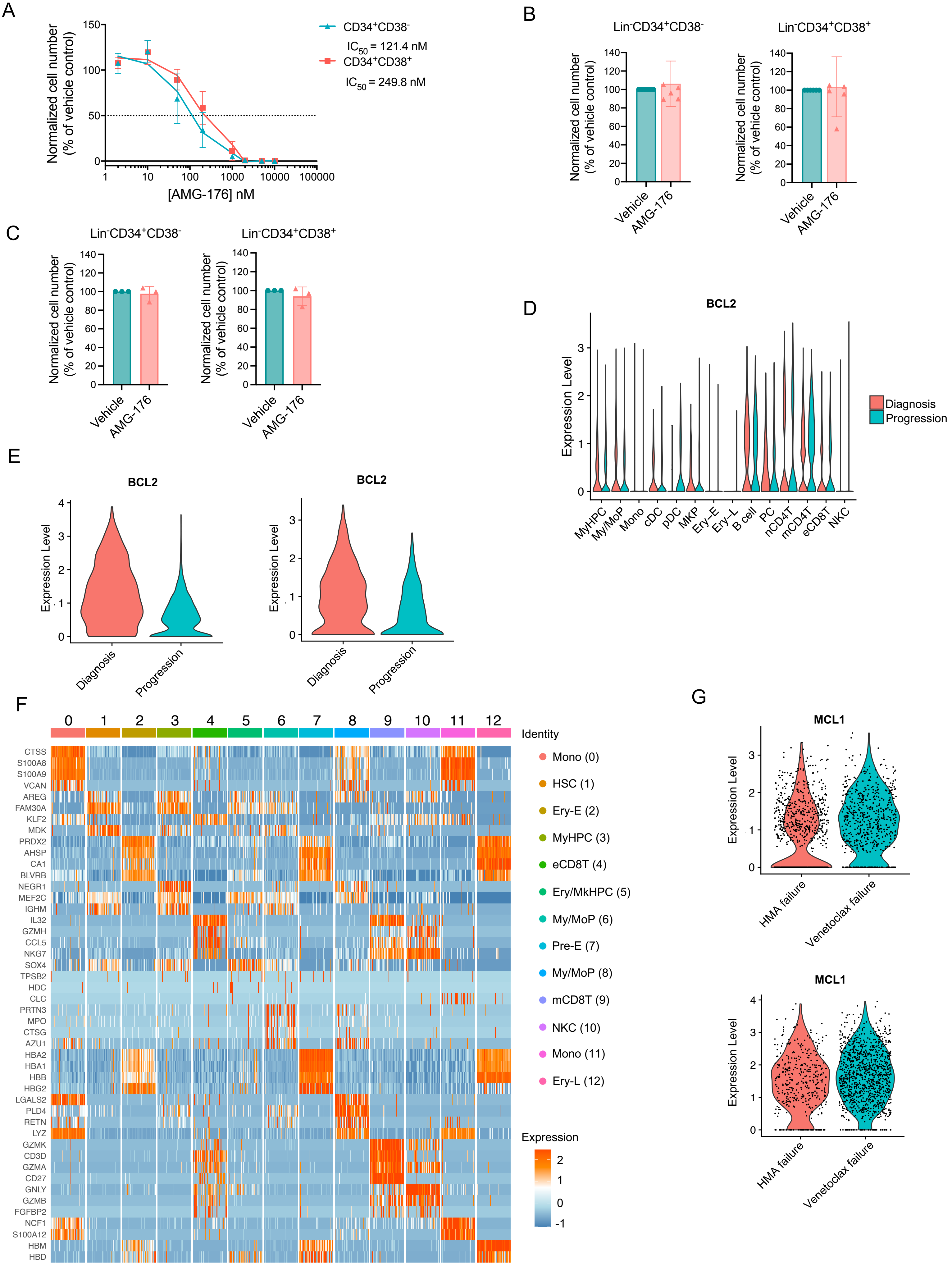
A
Normalized cell number (% of vehicle control)
150
100
50
0
1
10
100
1000
10000
100000
[AMG-176] nM
CD34$^+$CD38$^-$
IC$_{50}$ = 121.4 nM
CD34$^+$CD38$^+$
IC$_{50}$ = 249.8 nM
B
Lin$^-$CD34$^+$CD38$^-$
Lin$^-$CD34$^+$CD38$^+$
Normalized cell number (% of vehicle control)
140
120
100
80
60
40
20
0
Vehicle
AMG-176
C
Lin$^-$CD34$^+$CD38$^-$
Lin$^-$CD34$^+$CD38$^+$
Normalized cell number (% of vehicle control)
Vehicle
AMG-176
D
BCL2
Expression Level
MyHPC
My/MoP
Mono
cDC
pDC
MKP
Ery-E
Ery-L
B cell
PC
nCD4T
mCD4T
eCD8T
NKC
Diagnosis
Progression
E
BCL2
Expression Level
Diagnosis
Progression
BCL2
Expression Level
Diagnosis
Progression
F
0 1 2 3 4 5 6 7 8 9 10 11 12
CTSS
S100A8
S100A9
VCAN
AREG
FAM30A
KLF2
MDK
PRDX2
AHSP
CA1
BLVRB
NEGR1
MEF2C
IGHM
IL32
GZMH
CCL5
NKG7
SOX4
TPSB2
HDC
CLC
PRTN3
MPO
CTSG
AZU1
HBA2
HBA1
HBB
HBG2
LGALS2
PLD4
RETN
LYZ
GZMK
CD3D
GZMA
CD27
GNLY
GZMB
FGFBP2
NCF1
S100A12
HBM
HBD
Identity
Mono (0)
HSC (1)
Ery-E (2)
MyHPC (3)
eCD8T (4)
Ery/MkHPC (5)
My/MoP (6)
Pre-E (7)
My/MoP (8)
mCD8T (9)
NKC (10)
Mono (11)
Ery-L (12)
Expression
2
1
0
-1
G
MCL1
Expression Level
HMA failure
Venetoclax failure
MCL1
Expression Level
HMA failure
Venetoclax failure

Figure S10. *RAS* pathway mutated CMML cells, but not *RAS* pathway wildtype CMML cells, rely on *MCL1* overexpression to maintain their survival at BP. Related to Figure 4. (A) Number of live cultured Lin$^-$CD34$^+$CD38$^-$ and Lin$^-$CD34$^+$CD38$^+$ cells from HD BM samples (n=2) after 48 hours of treatment with AMG-176. Lines represent means ± SEMs. **(B)** Number of live Lin$^-$CD34$^+$CD38$^-$ HSCs and Lin$^-$CD34$^+$CD38$^+$ MyHPCs from *RAS* pathway mutant CMML patients at diagnosis and after treatment with vehicle or AMG-176 (n=6, 20nM) for 48 hours. Lines represent means ± SDs. A paired two-tailed Student t-test revealed no significant differences. **(C)** Number of live Lin$^-$CD34$^+$CD38$^-$ HSCs and Lin$^-$CD34$^+$CD38$^+$ MyHPCs from *RAS* pathway wild-type CMML patients at BP after HMA failure and after treatment with vehicle or AMG-176 (n=4, 20nM) for 48 hours. Lines represent means ± SDs. A paired two-tailed Student t-test revealed no significant differences. **(D)** Violin plots of *BCL2* expression levels across each *RAS* pathway mutant CMML MNC population at diagnosis compared with those at BP (no significant difference was detected). **(D)** Violin plots of *BCL2* expression levels in MyHPCs (left) and My/MoPs (right) from *RAS* pathway wild-type CMML at diagnosis compared with those at BP (adjusted $P = 5.45 \times 10^{-54}$ and 1.13×10^{-24}, respectively). **(F)** Heatmap of the expression levels of the top 5 genes enriched in each of the 13 clusters shown in Fig. 4E. **(G)** Violin plots of *MCL1* expression levels in *RAS* pathway mutant MyHPCs (top) and My/MoPs (bottom) at the time of BP after HMA therapy failure compared with those at venetoclax failure (adjusted $P = 1.12 \times 10^{-15}$ and no significant difference, respectively).